



**Politecnico  
di Torino**

**Politecnico di Torino**

Mechanical Engineering  
A.a. 2021/2022  
Sessione di Laurea Luglio 2022

**Determination of mechanical characteristics  
of sand core with inorganic binder through  
a correlation method between experimental  
tests and numerical simulations**

Relatori:

Prof. Carlo Rosso

Candidato:

Lorenzo Vannucchi



## Abstract

*This study is inserted in the engineering consultancy activity of DACA-I Powertrain Engineering and in particular it is part of a project ICARO that the company developed in collaboration with the metallurgical plant of Teksid SpA located in Carmagnola (TO).*

*The thesis work deals with the definition of mechanical characteristics of sand cores with inorganic binder used in gravitational die casting with aluminum alloy and permanent steel mold. Attention towards inorganic binders is growing up due to a lower hazardous gas generation and safer working condition during the casting process.*

*An initial experimental activity is carried out, it consists in a series of high temperature 3-point bending tests on bar specimens made of agglomerate material, special foundry sand linked with inorganic binder. A statistical approach is used to define the mechanical characteristics, exploiting the Weibull distribution function. The following part of the work consists in the realization of simulation activities to characterize material properties and in particular the interaction behavior of sand core with molten metal.*

# Summary

INTRODUCTION .....	1
1. PRODUCTION OF CORES .....	2
1.1 Hardening process .....	3
1.1.1 Chemical processes .....	3
CO <sub>2</sub> Forming .....	3
1.1.2 Physical processes .....	3
Convection heating .....	3
Microwaves .....	4
1.2 De-coring .....	5
2. SAND THERMAL BEHAVIOR SIMULATION .....	6
2.1 Geometry .....	6
2.2 Mesh .....	7
.....	7
2.3 Materials .....	7
Air .....	7
.....	8
Sand .....	9
2.4 Laminar simulation .....	10
2.5 First heating simulation .....	10
2.6 Second heating simulation .....	11
2.7 CFD-Post Activity .....	12
3. 3-PONT BENDING TEST FOR MECHANICAL CHARACTERIZATION OF SAND CORE MATERIAL .....	14
3.1 Specimen production technique .....	14
3.2 Instruments and devices .....	15
- Grips .....	15
- Climate chamber .....	15
- Testing machine .....	16
3.3 Procedure .....	17
4. Data post-processing .....	17
4.1 Approach 1 .....	18
4.1.1 Statistical analysis .....	21
Linear regression method .....	22
Maximum likelihood method .....	24
Results .....	24
4.1.2 Simulation, geometry and settings .....	25
4.2 Approach 2 .....	27
4.2.1 Simulation .....	27
4.2.2 Statistical analysis .....	28

Poisson coefficient .....	29
4.3 Friction effect error in flexural testing .....	29
5. METAL-STATIC SIMULATION .....	31
5.1 Fluent geometry .....	31
5.2 Fluent setup .....	31
5.3 Fluent results .....	32
5.4 Static Structural .....	32
6. DYNAMIC-METAL FORCE SIMULATION .....	34
6.1 Fluent geometry .....	34
6.2 Fluent setup .....	34
6.3 Fluent results .....	35
6.4 Static Structural .....	38
7. SOLIDIFICATION SIMULATION .....	39
7.1 Fluent geometry .....	39
7.2 Materials .....	40
Steel .....	40
Coating .....	40
Aluminum alloy .....	40
7.3 Setup .....	41
7.3.1 Initial condition .....	42
7.3.2 Boundary condition .....	42
7.4 Fluent results .....	43
7.5 Static Structural .....	46
8. CONCLUSION .....	48
REFERENCES .....	49

# INTRODUCTION

This work thesis has been developed thanks to the internship activity with the company DACA-I Powertrain Engineering and it deals with an experimental and numerical correlation of mechanical characteristics of sand cores produced with inorganic binder.

In metal casting industry sand cores allow the production of complex geometry components ensuring holes and cavities generation with both functional and weight-saving purposes also in high volumes production. Cores are composed in general by a filler and a binder. The filler is a specific sand for foundry applications and the binder is a chemical compound with organic or inorganic origin and it fix the grains together. Additives are usually necessary to guarantee the required characteristics. Depending on casting technique, the core can be completely integrated into the casting mold or loosely laid therein. After solidification of the metal, the die is taken apart and the cast product is released. Later the core is broken, removed from the product and usually disposed of, although there have been applications for re-usable cores. Here below a general scheme of process chain is reported (Figure 1).

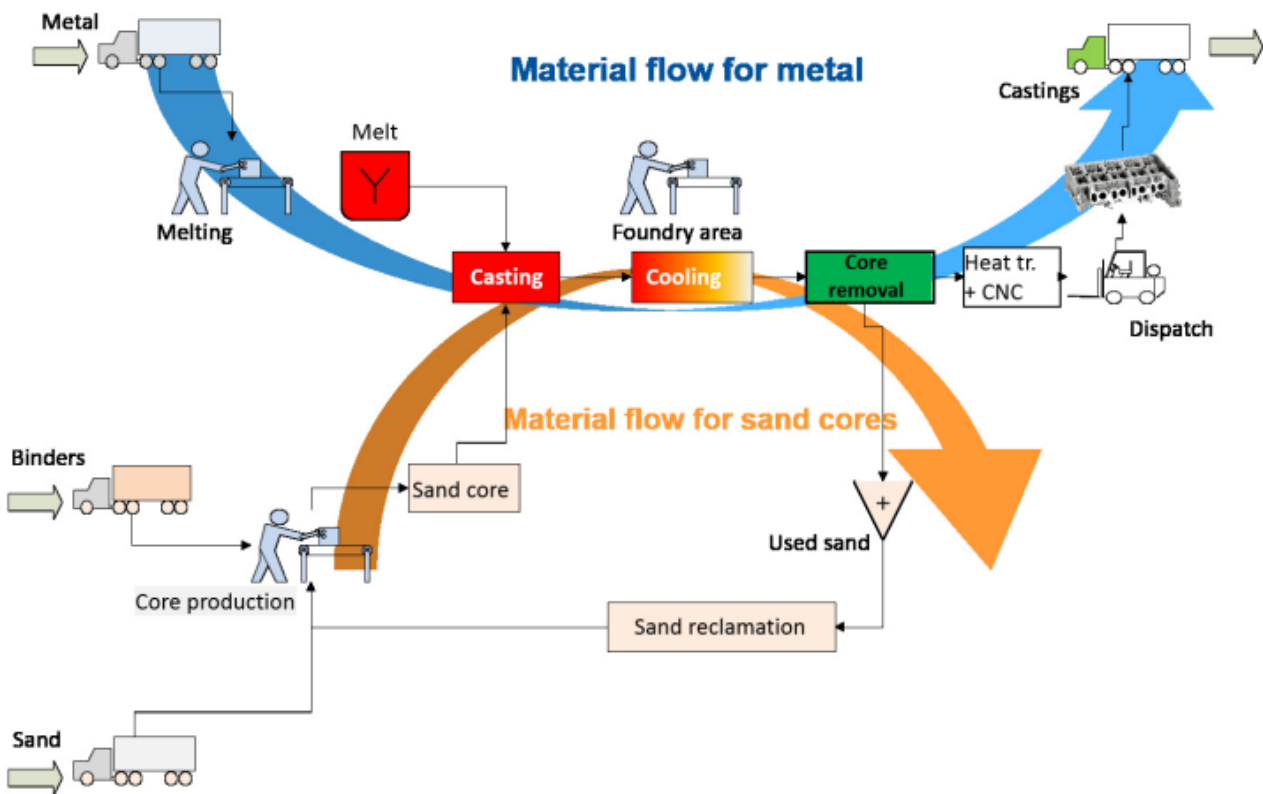


Figure 1: scheme of process chain for metal casting application

The casting cores must withstand tough requirements which depend on casting technique and alloy used and the main are [11]:

- Sufficient strength to allow handling and manipulation operations
- High resistance against humidity during core storage
- High erosion and penetration resistance and no chemical interaction with the cast metal to deliver a good casting surface quality
- Low gas evolution and high gas permeability to avoid casting defects
- High bending strength, which is the most critical load condition due to clamping and thermal loads

- Easy shake-out after casting to obtain sand-free cast parts
- A good recycling ability of used foundry sand
- Environmentally friendly core systems with low odor development

In order to satisfy as much as possible all these tasks and paying attention to health and safety guidelines and environmental impact reduction, inorganic binders have been implemented since they are odorless and emission free. Organic binders have some limits during both core forming and casting procedures: because of high temperature, the organic binder combusts decomposing into gases such as  $CO$ ,  $CO_2$  and, in the case of incomplete combustion, also generating tar or soot, which must be removed from the die and work devices increasing process time and maintenance need. Furthermore, the huge amount of volatile species emitted contributes to increase porosity that affects structural integrity.

For all these reasons inorganic binders are attractive, in fact the absence of combustible and potentially hazardous products evolving during the casting process is a main driving force to implement inorganic binders in high volume production. If on one side this feature is positive on the other hand the lack of combustion products derives mainly by a poor thermal degradation which is linked with a worse core removal ability if compared with organic binders. A further limit that affects cores with inorganic binders is the tendency to absorb humidity during storage that worsen mechanical properties and that can be released during casting operation reducing also cast part quality. For these reasons it is fundamental to avoid keeping cores in wet and hot environmental condition for a long time. [13]

## 1. PRODUCTION OF CORES

The production strategy of cores is a key point in the entire casting process. High quality, high strength, low cost and possibly low environmental impact are some of the crucial requested characteristics. The main core features, that a making process should provide are [4]:

- excellent dimensional accuracy
- clean and smooth surface
- high thermal stability
- good shakeout

The mechanization of the process consists of almost solely in the usage of core blowing machines. Cold-box, hot-box and warm-air technologies require that core blowing machines shall be additionally equipped with either core-box, pre-heating system or gas purging and neutralization system, or hot air purging systems. Optimization of a core production process by shooting consists in the selection of working parameters of the filling of the core-making machine and compaction of molding sands as well as methods of sands hardening by means of gaseous or thermal agents.

The entire production can be mainly divided in four consecutive steps:

- Mixture preparation: sand, binder and additives are mixed for a certain time to assure a uniform distribution of all components
- Forming: the mixture is fitted in the core box blown by the core-blowing machine through one or more nozzles with a certain pressure. Core box is usually an iron or aluminum container for the mixture with the specific core-shape. Before the process begins some chemical products are applied on the inner surfaces of the box to make the extraction of the sand core easier

- Hardening: the core assumes better mechanical capability thanks to a specific reaction which depends on the nature of both the binder and the agent
- Core coatings can be used on the external surfaces to prevent infiltration of the molten metal into the core body and to allow easy separation of the sand core from the cast product

## 1.1 Hardening process

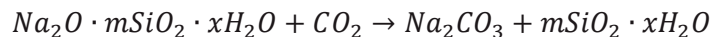
Considering inorganic cores, a great differentiation can be done based on the nature of the hardening process which can be chemical or physical. In the former case the mostly used is the  $CO_2$  forming or alternatively chemical hardeners usage while in the latter case hot air blowing, convection heating or micro-waves are the main possible options. Any hardening process must guarantee a satisfying strength, usually about 2 MPa, to allow manipulation during the whole process.

### 1.1.1 Chemical processes

The most common chemical process is  $CO_2$  forming, it is a cold hardening procedure and in general the amount of water removed from the mixture is quite low and for this reason vapor evolution is huge.

#### *CO<sub>2</sub> Forming*

A  $CO_2$  gas flux passes through the mixture while it is in the core box. The reaction



provides the formation of silica hydrogel bonds between sand grains and they assure necessary cohesion and rigidity to allow demolding and handling. Flux should be induced homogeneously in the whole volume to achieve the best result. Some additives can be added to make the reaction faster, to improve shakeout properties or mixture compaction. This process is characterized by numerous advantages as its relative low cost, absence of dangerous equipment, good dimensional accuracy, adequacy for a wide range of core shapes and size and a high level of mechanization. On the contrary the main limitations are the low strength of the hardened sand, poor breakdown of the sand after casting, difficult reclamation of the used sand and sensibility to environmental humidity and temperature, so great attention must be kept in assuring sufficient workbench life.

### 1.1.2 Physical processes

With respect to  $CO_2$ , physical approaches assure a much greater improvement of core mechanical properties. These procedures are mainly based on the dehydration of the mixture generating a dehydrated layer of vitreous sodium silicate ( $Na_2O \cdot mSiO_2$ ) and so forming durable bridges linking the matrix grains. The reaction is partly invertible so it is particularly important to store the formed cores in a controlled environmental condition because in a too wet and hot site cores absorb humidity that deplete mechanical properties and that will be released during casting, worsening the quality of the metal product.

#### *Convection heating*

The hardening process happens thanks to the great amount of heat released to the mixture by conductive-convective heat exchange, so the core becomes previously harder in the superficial layers and then hardening proceeds deeper and deeper.

## Microwaves

Microwaves cause dielectric polarization of water molecules causing a general volumetric heating. The generated steam passes through the core thanks to its permeability. This process has some advantages as the great amount of energy and time saved and the great increase in strength (Figure 3) of the mixture that also gives the possibility to make thinner cores if necessary. Chemical processes (Figure 2a) can need lots of hours to obtain acceptable mechanical performances while traditional convection hardening needs long time and great amount of energy. The main disadvantage of microwaves technique consists in the necessity of a more complex control system which complicates the set-up. Furthermore, the core box material must be microwaves permeable as Teflon, glass or special kind of concrete [10].

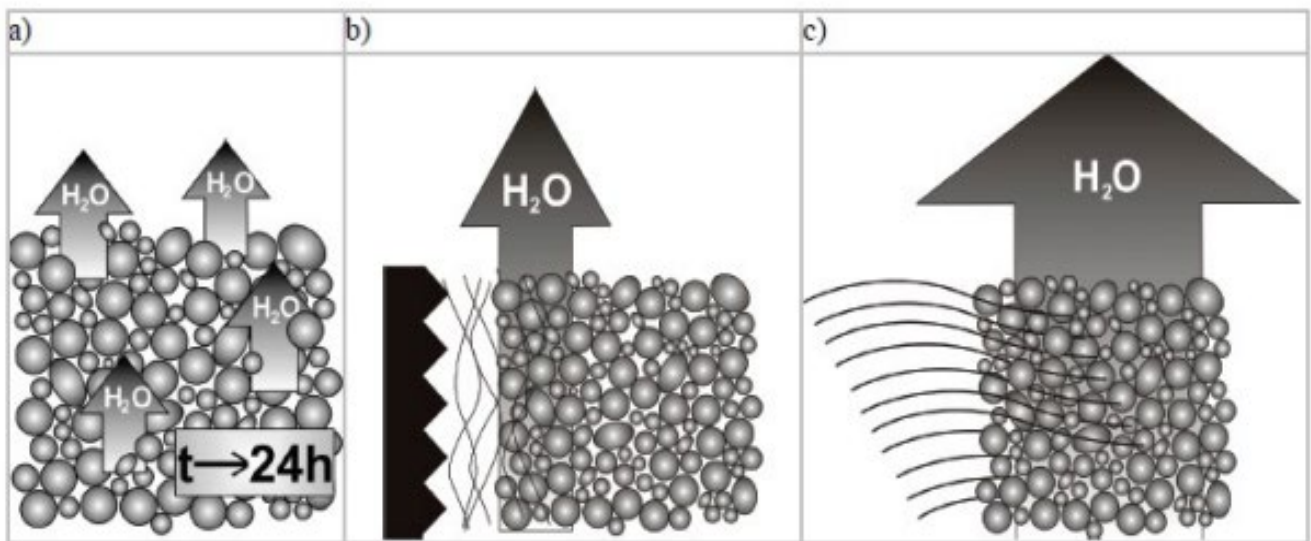


Figure 2: schematic figure of hardening processes: a) chemical process; b) convection; c) micro-waves

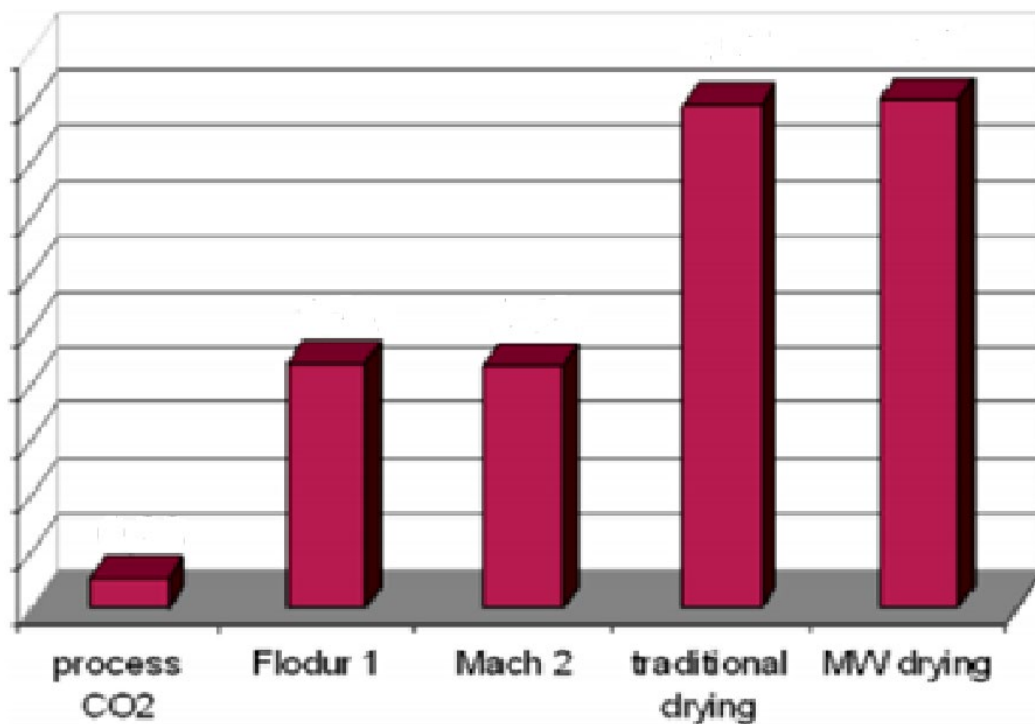


Figure 3: qualitative comparison of bending strength for different kinds of hardening processes

## 1.2 De-coring

At the end of the solidification and cooling of the component, a sand core removal process is required to obtain a sand-free casting. Inorganic sand cores show in general a lower thermal degradation if compared with organic binders due to their non-combustible nature, so they have a worse removal ability. Thermal degradation of organic binders occurs due to the pyrolysis that degrades adhesive bonding among sand grains and making them fragile. Inorganic binders generally show a completely different behavior, in fact a retained strength after thermal exposure is generally present. Furthermore, in Al-castings, due to the lower achieved thermal loads, usually more effort has to be put into the removal of sand cores from the castings. Core break-down behavior is generally influenced by:

- Design of casting as number and size of openings
- Selection of core sand and binder
- Baking, because not fully hardened cores are more difficult to remove
- Thermal exposure, in fact in general higher the introduced heat, easier the core destruction

## 2. SAND THERMAL BEHAVIOR SIMULATION

In this section two similar simulations are presented, both deal with the heating of a sand bar core inside an oven. The main proposal of these simulations is the time evaluation, requested to provide a homogeneous temperature distribution in the bar, avoiding great thermal gradients between the external surface, directly in contact with the hot air inside the oven, and the inner core region.

### 2.1 Geometry

Geometry is constituted by a squared section specimen, whose dimensions are  $170 \times 22.4 \times 22.4 \text{ mm}^3$ , all surrounded by a certain volume of air ( $237.2 \times 78.4 \times 78.4 \text{ [mm}^3\text{]}$ ). To reduce the complexity of the problem and computational effort symmetry is exploited: both longitudinal and transversal planes are symmetry planes as shown in Figure 4. This volume reduction is perfectly in accordance with the symmetrical behavior of the analyzed volume, while the third possible symmetry (plane XZ) cannot be considered. In accordance with the symmetrical volume reduction sand bar dimensions are shown in Figure 5. The surrounding volume of air is large enough to make negligible the presence of the bar on the air behavior beyond the boundary of the control volume.

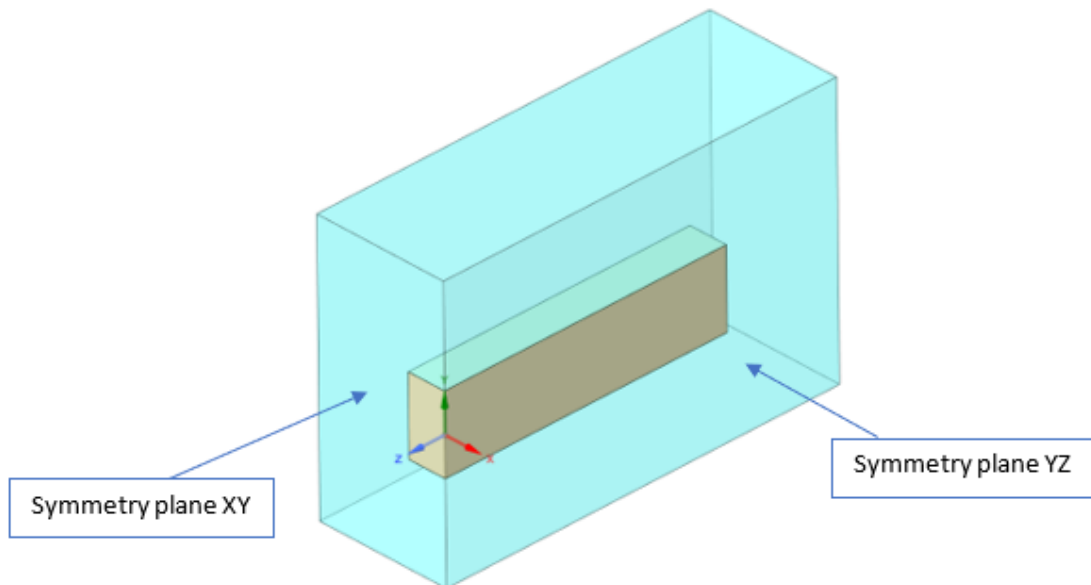


Figure 4: analyzed geometry and symmetry planes

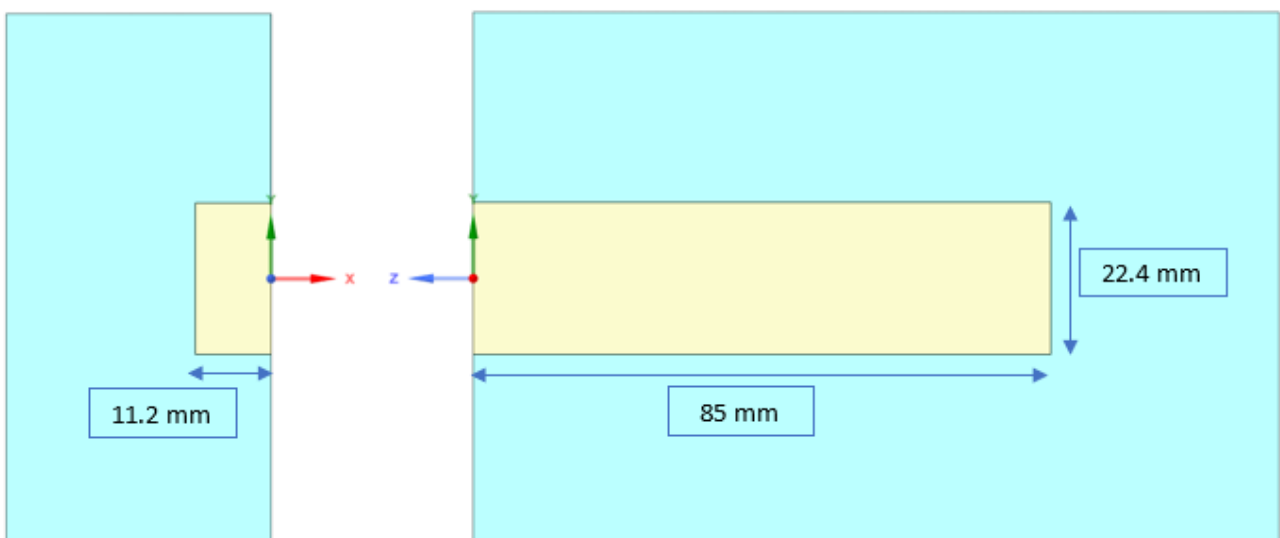


Figure 5: Side (plane YZ) and front (plane XY) views of the volume and relative dimensions of sand bar

## 2.2 Mesh

In the air volume the mesh dimension is variable: from the external walls, where it is set equal to 10 mm, to the air-specimen interface surfaces where it is 1 mm. This decreasing setup provides more accurate information in the heat exchange zone (Figure 6). For the same reason in the entire volume of the specimen mesh dimension is equal to 1 mm and the thickness of the layers of elements of air in correspondence of the interface is reduced (Figure 7).

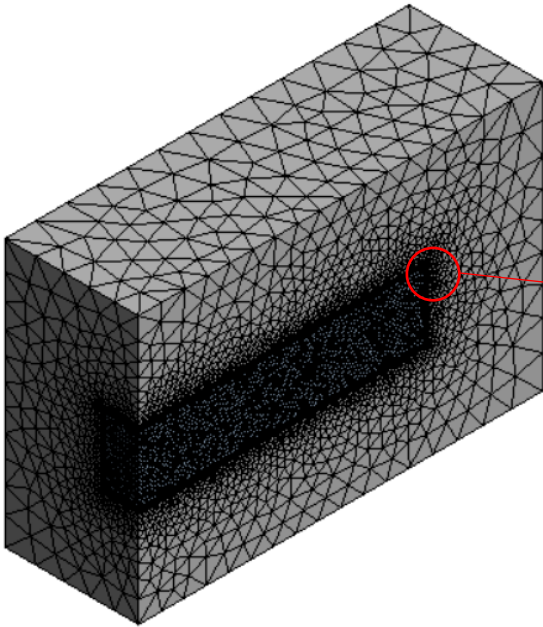


Figure 6: mesh of the entire volume

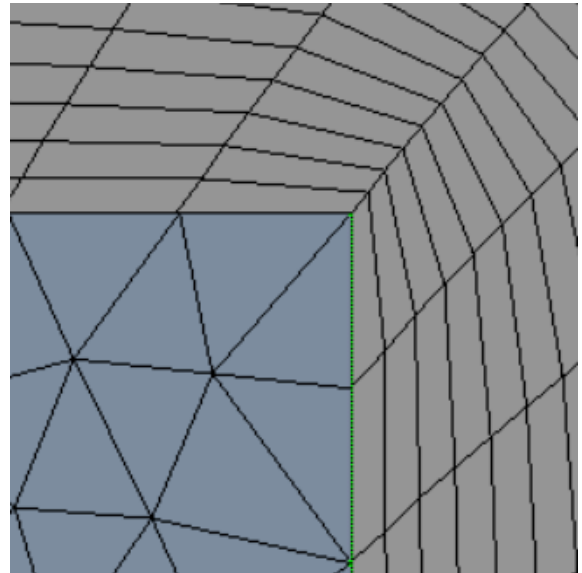
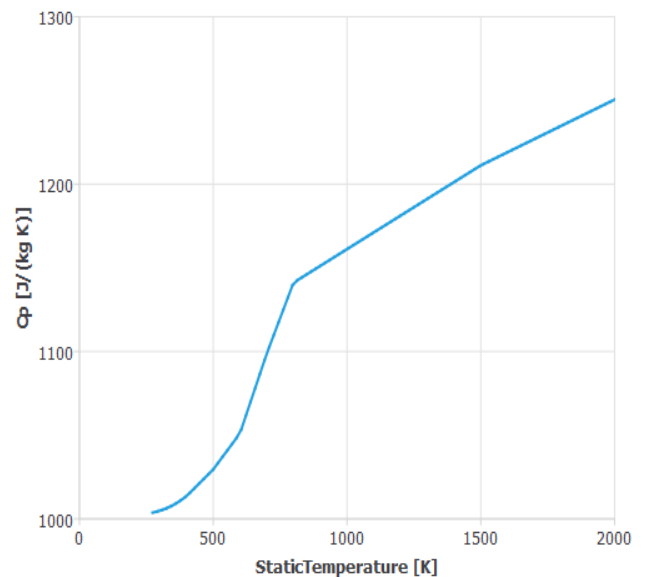
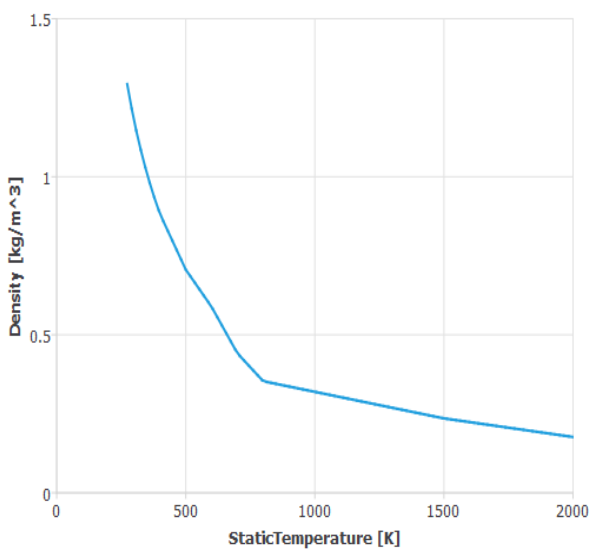


Figure 7: focus on the inflation at the interface

## 2.3 Materials

Sand and air have characteristics of material dependent by temperature. Thermal conductivity and specific heat coefficient, for both materials, and viscosity and density, only in case of air, have been defined through a piece-wise linear functions.

Air



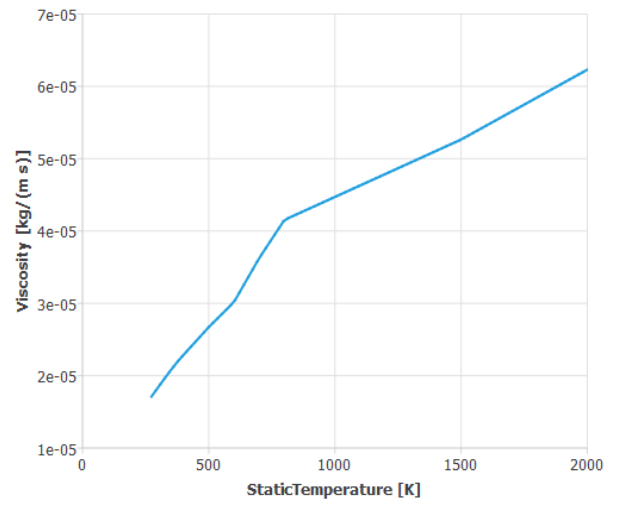
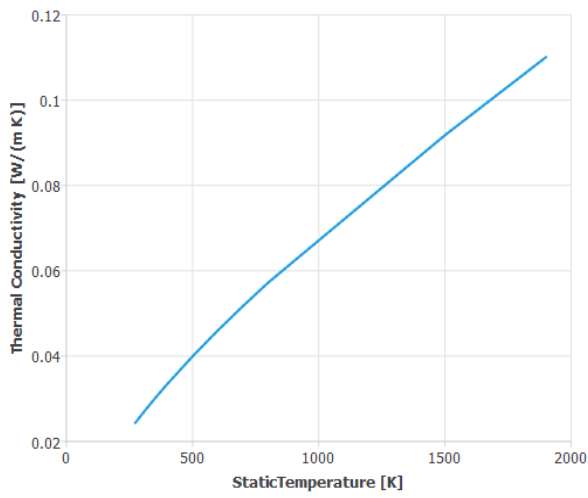
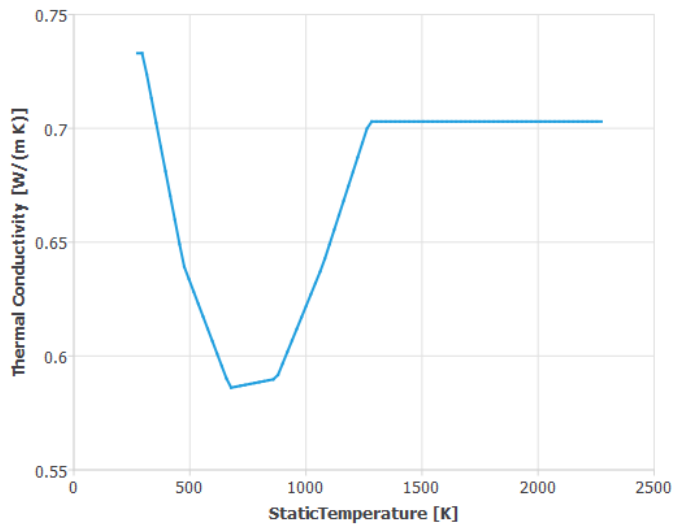


Figure 8: plots of air characteristics

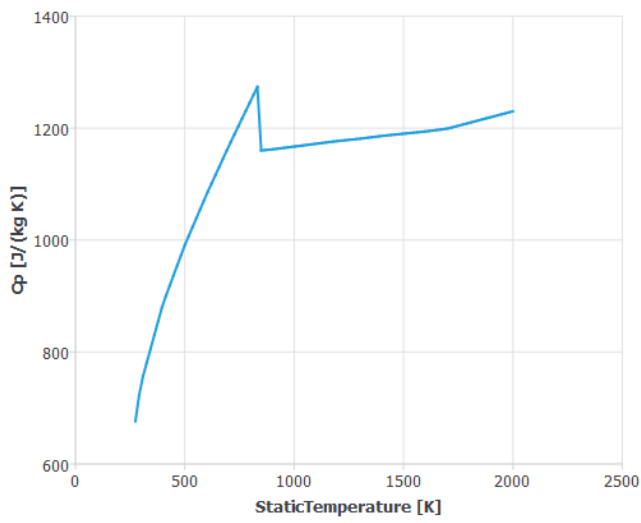
T [K]	$\rho$ [kg/m <sup>3</sup> ]	Cp [J/kg K]	Th cond [W/m K]	Visc [10 <sup>-5</sup> kg/m s]
273,15	1,293	1003,7	0,02436	1,71
283,15	1,247	1004,1	0,02512	1,76
288,15	1,225	1004,3	0,0255	1,78
293,15	1,205	1004,5	0,02587	1,81
303,15	1,165	1005	0,02662	1,86
313,15	1,127	1005,5	0,02735	1,90
333,15	1,06	1006,8	0,0288	2,00
353,15	1	1008,4	0,03023	2,09
373,15	0,946	1010,4	0,03162	2,18
400	0,8824	1013,5	0,03345	2,29
500	0,706	1029,5	0,03994	2,67
600	0,5883	1051,1	0,04601	3,02
700	0,4412	1098,7	0,05175	3,62
800	0,353	1141,1	0,05725	4,15
1500	0,2353	1211,2	0,09179	5,26
2000	0,1765	1250,5	0,11007	6,23

Table 1: temperature dependent characteristics of air

# Sand



T [K]	Th cond [W/m K]
274	0,733
297	0,733
473	0,64
673	0,586
873	0,59
1073	0,64
1273	0,703
2273	0,703



T [K]	Cp [J/kg K]
274	676
298	741
400	886
500	991
600	1082
700	1167
800	1248
846	1285
847	1160
900	1162
1000	1167
1100	1172
1200	1177
1300	1181
1400	1186
1500	1190
1600	1194
1700	1199
2000	1230

Figure 9: plots of sand characteristics

Table 2: temperature dependent characteristic of sand

## 2.4 Laminar simulation

To verify the laminar flow hypothesis a brief additional simulation has been set and the Reynolds number, only after one second of heat exchange, has been considered (Figure 10). The value is really low in the entire air volume and so the fluid flow can be considered laminar. It is sufficient to make this analysis only in the first second of heat exchange because in all the following instants the temperature difference between air and sand will be lower and lower and so the air velocity and, as consequence, the Reynolds number decrease.

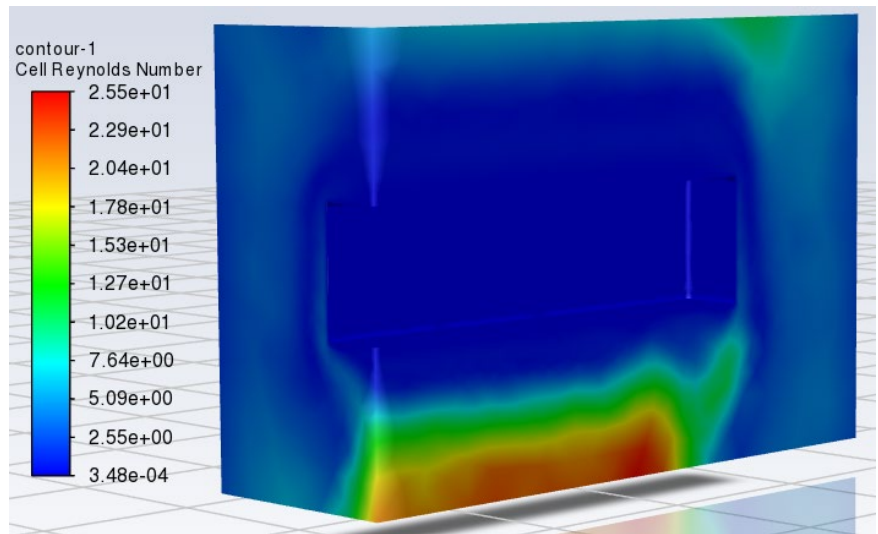


Figure 10: Reynold number distribution in the air volume

## 2.5 First heating simulation

This first simulation is characterized by a stable temperature of the air in the oven equal to 623.15 [K] (350 °C) and so, in the considered volume, air is cooled by the presence of the specimen and moves down because the temperature of the air just outside is imposed constant and equal to the initial one: the fluid outside the analyzed volume is not affected by the presence of the specimen. Some further hypothesis and simplifications have been done:

- In this model the contact between the specimen and the bearings in the oven to maintain the specimen in the right position are not considered. Neglecting this kind of contact the entire heat exchange is performed only through convection.
- The simulation starts with the air of the oven at the stable temperature imposed with the specimen at the environmental one and the increasing temperature phase after the power on of the oven is neglected.
- According to previous simulation laminar fluid flow is considered.

The initial condition imposed in the simulation are the initial temperatures of the specimen, equal to 298.15 [K] (25 °C), and air 623.15 [K] (350 °C).

The aim of the simulation is defining how long the heating time should be in order to annihilate as much as possible the temperature difference between specimen and air, and the temperature gradient between the core and the heat exchange surface of the specimen. 150 minutes is the simulated time and it satisfies previous requests in fact the temperature of the specimen appears homogeneous and only some degrees lower (about 2 [K]) than the air temperature as the following pictures show.

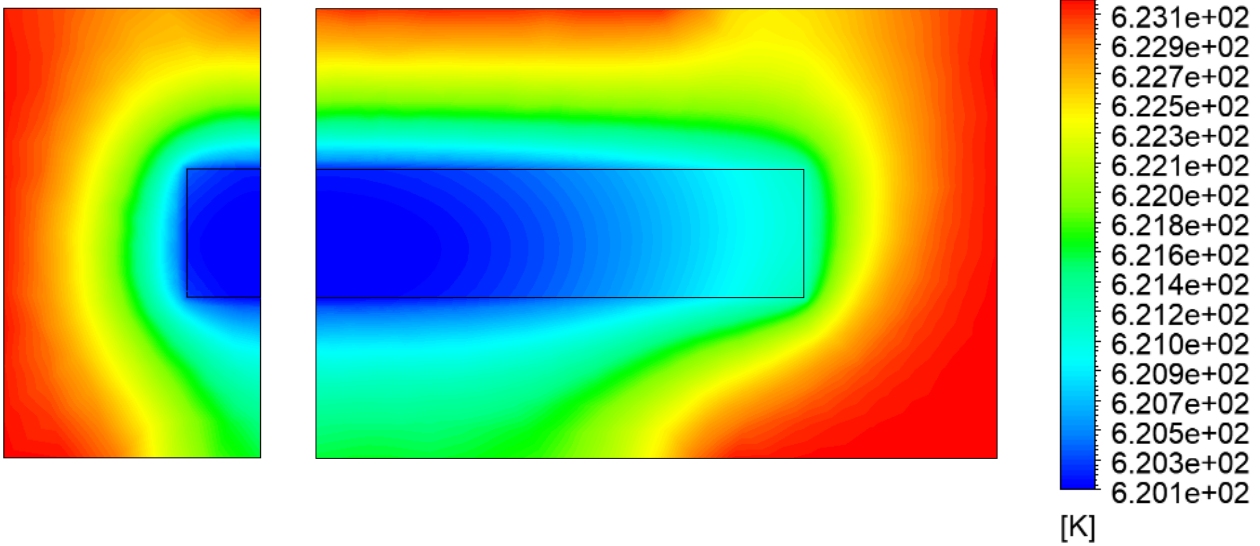


Figure 11: Front and side view of temperature distribution

Figure 12: Static Temperature legend

## 2.6 Second heating simulation

This second simulation has been performed following the same procedure with respect to the first one. The unique difference is the imposition of the air temperature in the oven that also in this case is equal to the initial one of air, equal to 523.15 [K] (250 °C). The total time needed, to obtain similar homogeneous conditions also in this case, results to be equal to 150 minutes.

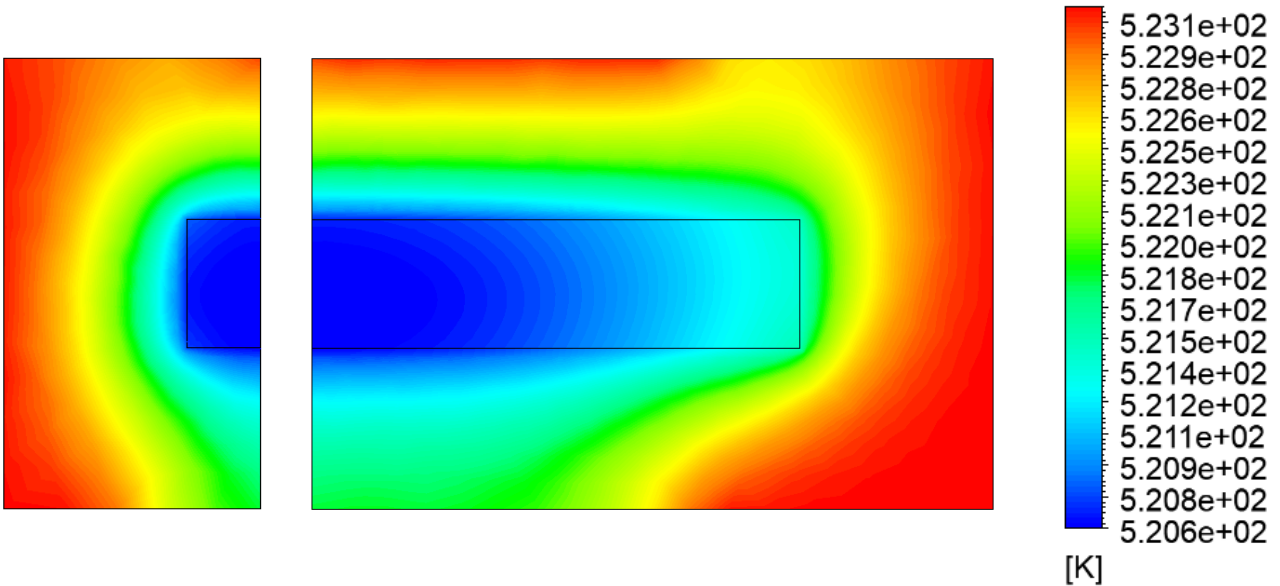


Figure 13: Front and side view of temperature distribution

Figure 14: Static Temperature legend

## 2.7 CFD-Post Activity

In this further analysis the temperature evolutions for both previous simulations have been built: some nodes in the specimen have been chosen to understand how temperatures in these specific points change and to make a comparison with the mean temperature of the entire volume of the specimen. In the following pictures the locations of the nodes and the associated temperature evolution are showed.

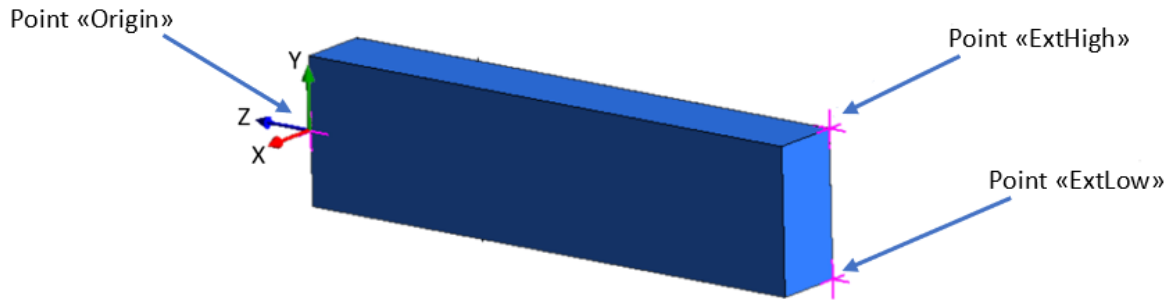


Figure 15: Nodes in the quarter specimen volume

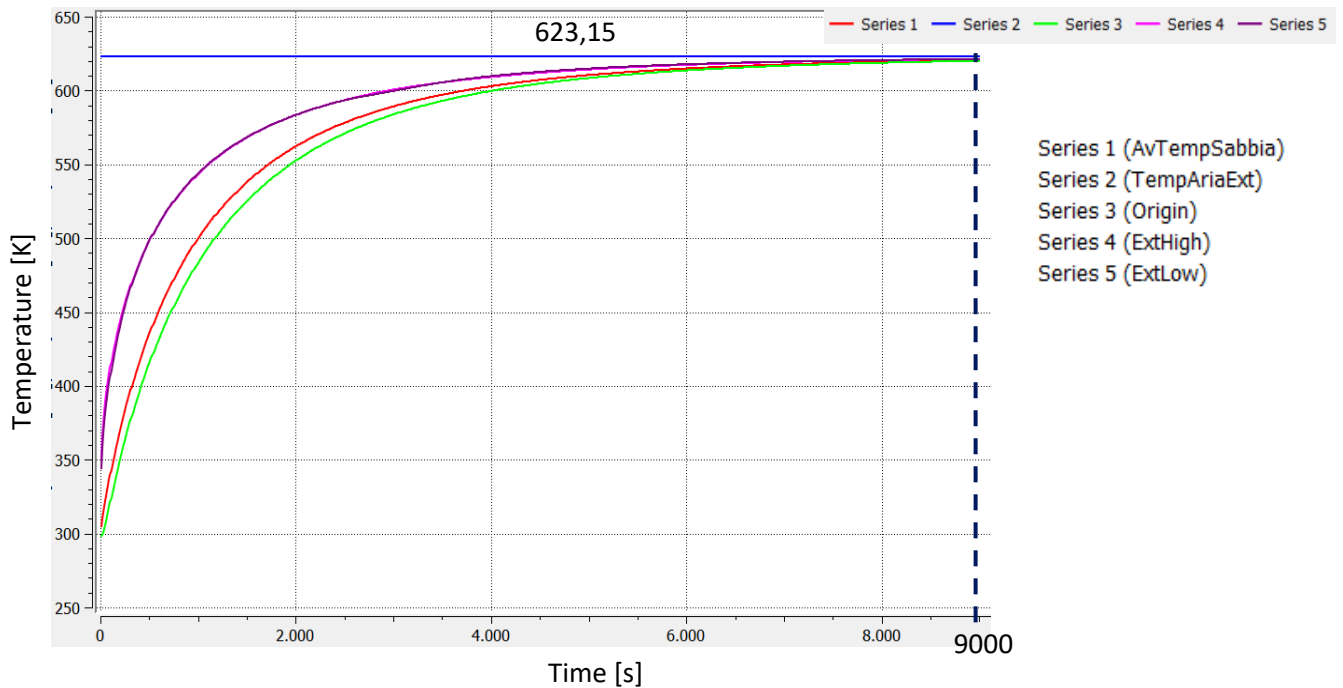


Figure 16: temperature evolution in the nodes and the mean

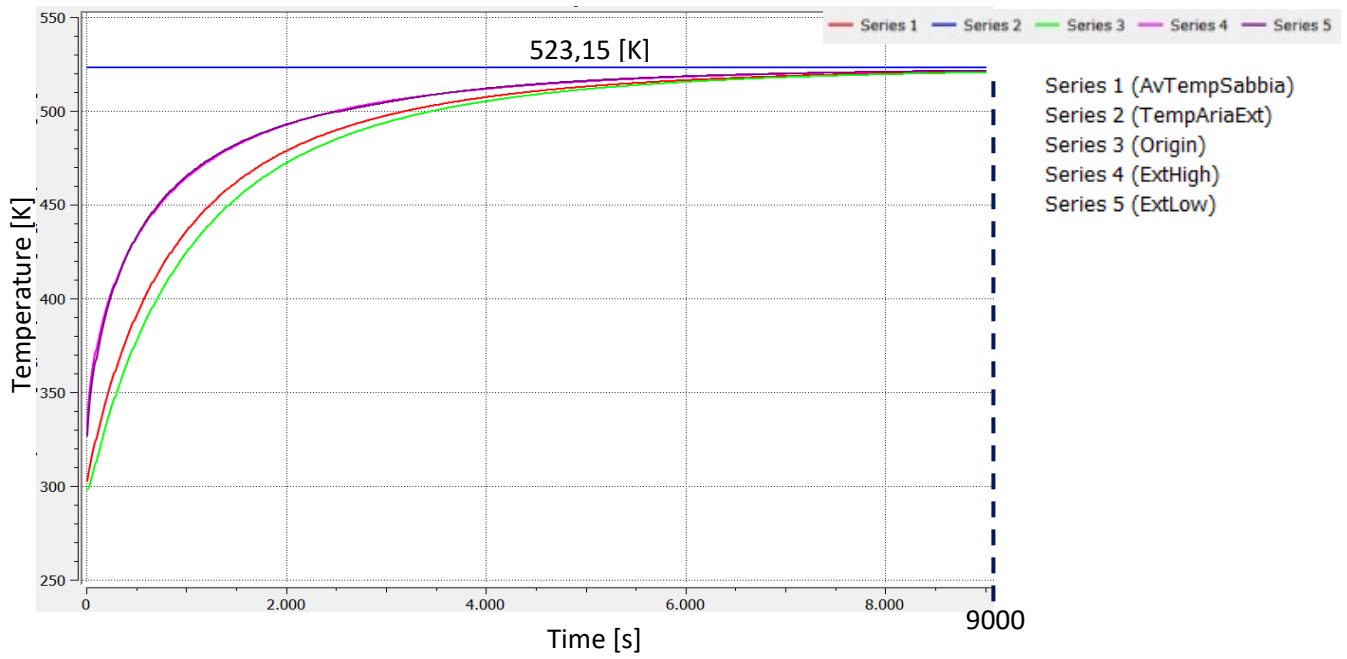


Figure 17: temperature evolution in the nodes and the mean temperature

Figures 16 and 17 underline that the simulated time is long enough to guarantee homogeneous temperature.

### 3. 3-PONT BENDING TEST FOR MECHANICAL CHARACTERIZATION OF SAND CORE MATERIAL

Three-point bending test is one of the methods used to determine the mechanical characteristics and influences of various parameters on mechanical performances of sand cores. The specimen is laid on two fixed external bearings and loaded in the midway by a punch. The test is strain controlled and the force applied is directly measured through an acquisition data system.

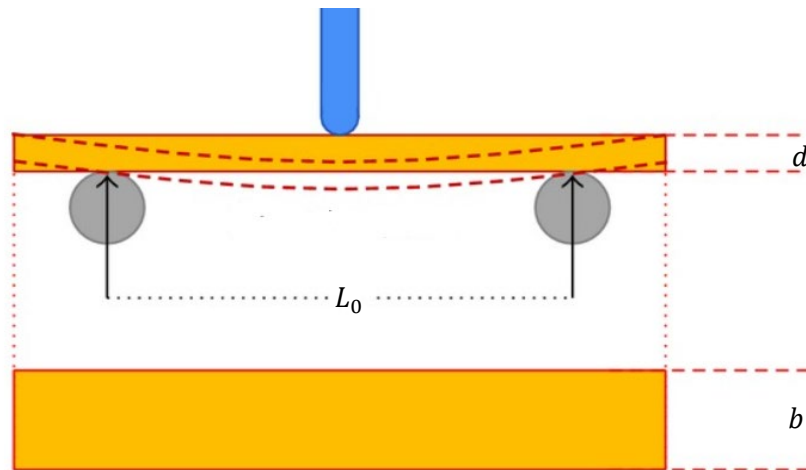


Figure 18: 3-point bending test scheme and dimensions

In order to define material characteristics and behavior, twelve 3-point bending tests have been performed and each specimen dimensions are  $170 \times 22.4 \times 22.4 \text{ mm}^3$ . Each test has been performed in certain temperature condition, reached through a climate chamber. Four different temperatures have been set:  $100 \text{ }^\circ\text{C}$ ,  $200 \text{ }^\circ\text{C}$ ,  $275 \text{ }^\circ\text{C}$  and  $350 \text{ }^\circ\text{C}$ , and for each one three specimens have been used. In addition to the data, obtained through direct experimental tests, others about different temperature conditions have been provided to have a wider and more complete thermal range: data about room temperature ( $25 \text{ }^\circ\text{C}$ ) and  $480 \text{ }^\circ\text{C}$  have been also considered.

#### 3.1 Specimen production technique

The twelve specimens needed to perform all the tests have been produced starting from the mixture of sand with CORDIS sodium-silicate aqueous solution (binder) with the addition of powdered Anorgit additive. The core-box is pre-heated at  $150 \text{ }^\circ\text{C}$  in such a way that a hardened external shell is formed. Later also the core is hardened with a gassing hot air flux at  $150 \text{ }^\circ\text{C}$  for 30 seconds. Through this production process the water glass is hardened in a purely physical way by means of evaporation of water. The used mixture is composed by 2.6% in weight of binder and 1.61% of additive. Before starting production, sand is warmed to enhance hardening reaction and to avoid slowing it down [6].

### 3.2 Instruments and devices

- Grips: the use of mechanical wedge grips, rather than hydraulic ones, is mandatory for high temperature application like in this case because the hydraulic ones are not suitable to work in so high temperature condition. On both grips, grip jaws and specific devices for the test are fixed together. The fastening of all these components is assured tightening the four screws on each grip, the lateral body slides down (vertical arrows) and the wedges moves one towards the other (horizontal arrows) clenching devices for the test.

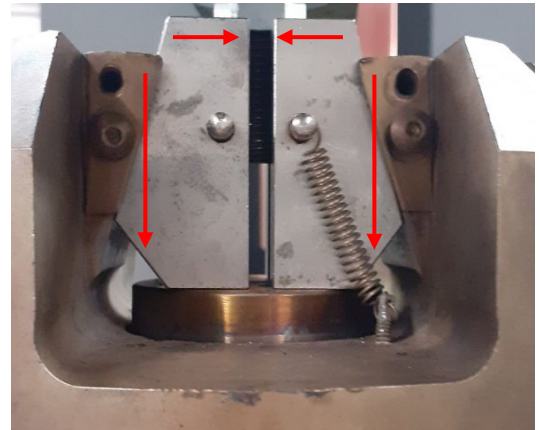


Figure 19: Grips and wedges tightening motion

- Climate chamber: to provide optimum heating rate, reducing thermal gradients and assuring thermal stability, hot air circulates around the specimen and grips. Ambient air enters from the rear of the chamber, most of that is heated passing across an electrically supplied element and conveyed in the chamber by fans, while the remaining part flows from the rear of the chamber into the space between the insulation and the outer panels, keeping cool the outer skin of the chamber. The temperature inside the chamber is monitored by a thermocouple. A triple-pane glass window on the opening door and a light inside the chamber provide visibility of the process also when the chamber is closed. The picture shows the main structure and air way. The climate chamber highest reachable temperature is equal to 350 °C. The chamber is mounted on roller brackets to slide it towards the testing machine and perform the test directly inserting the jaws in the chamber.

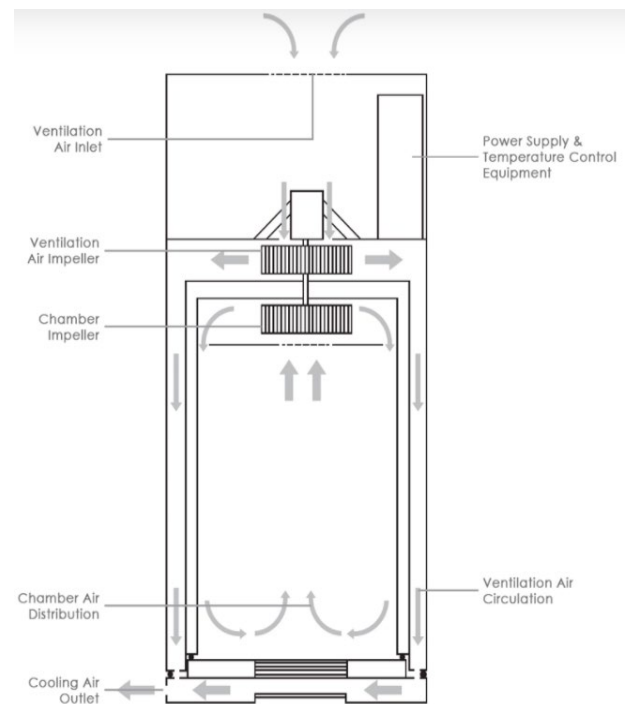


Figure 20: climate chamber structure and air flow directions

- Testing machine: servo-hydraulic testing system ideally suited for fatigue testing and fracture mechanics, driven by double-acting actuator with a stroke of  $\pm 75$  mm. Twin column structure to guarantee highest stiffness and best precision alignment. In Figure 22 some of the main dimensions are reported.

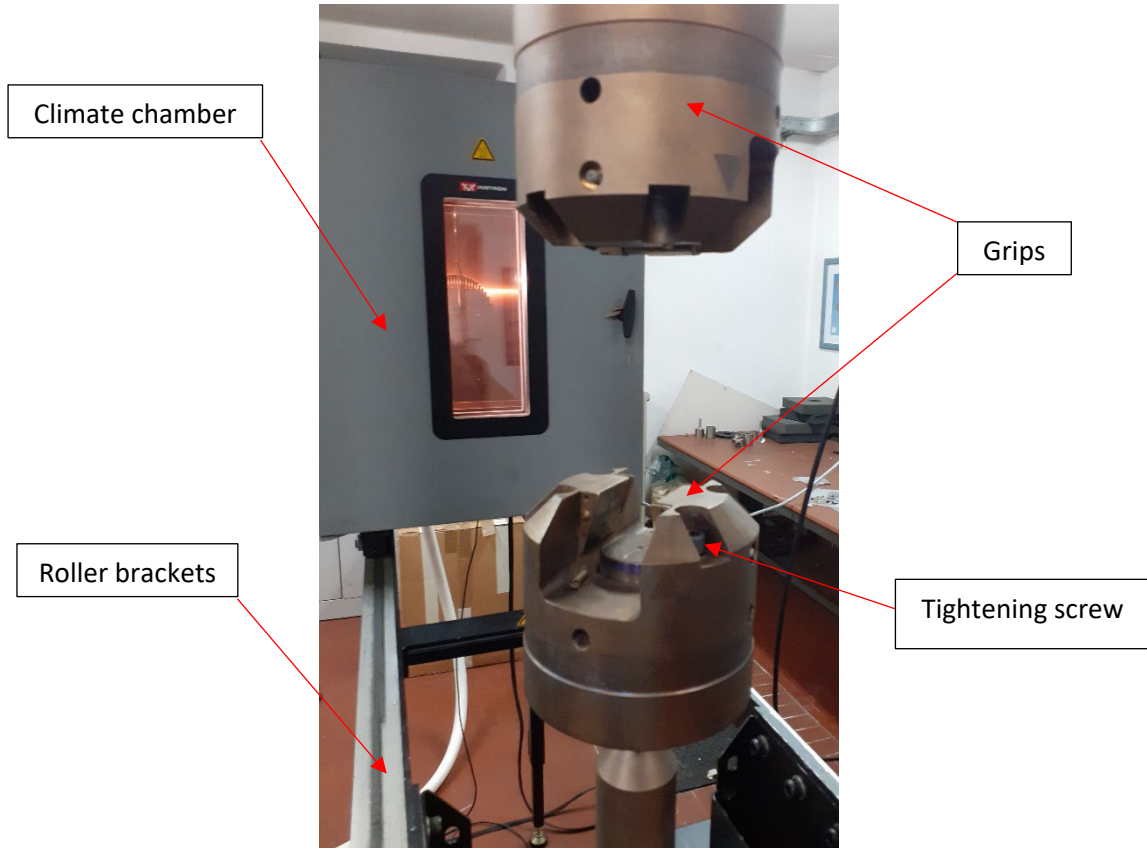


Figure 21

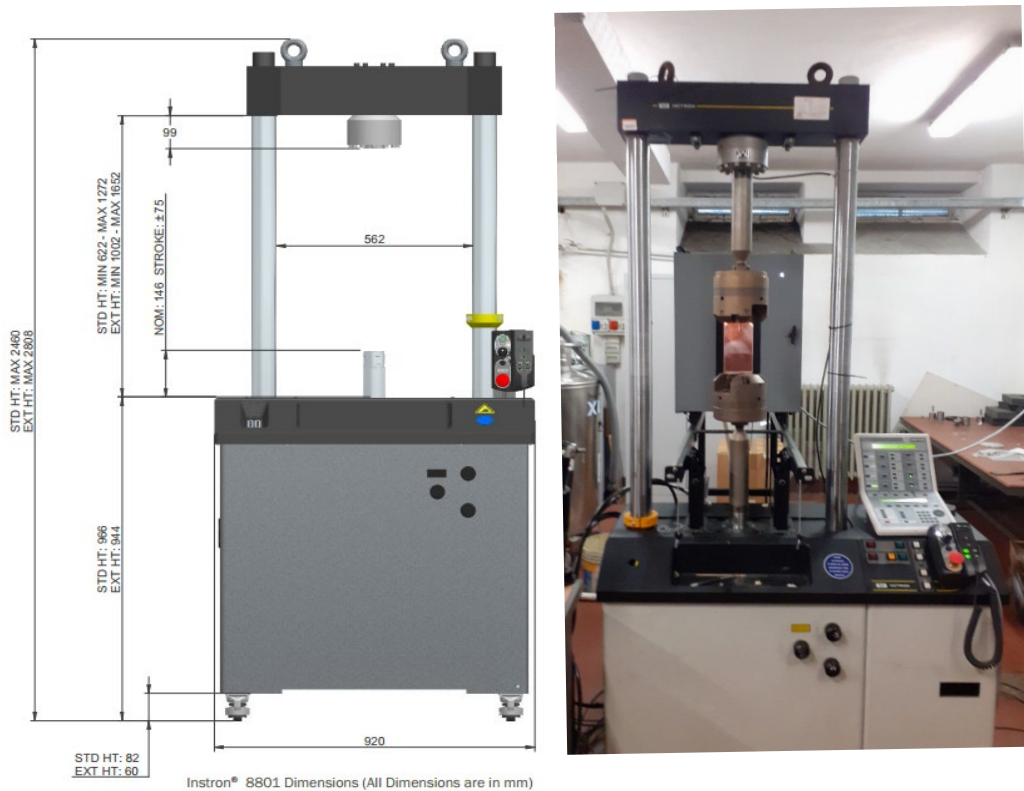


Figure 22: main dimensions of testing machine

### 3.3 Procedure

As first step all the twelve specimens have been arranged on the climate chamber floor in four groups of three: two of them leaning in parallel on the ground, and the third laid on them. Between the two on the base a certain air film has been assured to provide a more uniform heating (Figure 23). The climate chamber temperature has been set equal to 100 °C and the heating phase lasts about two hours. While the heating was proceeding the testing system has been prepared, fixing the grip jaw faces in the grips. On the lower grip the bearings, where the two ends of the specimens are in contact (Figure 24), are fixed, while on the upper grip a rounded corner shaped plate has been fixed and it applies the load about in the middle section.



Figure 23: specimens' arrangement in the climate chamber



Figure 24: lower grip arrangement

At the end of the heating phase the whole testing system has been moved in the climate chamber. The strain rate has been imposed equal to 5 mm/min and each specimen has been loaded until its breakage. Time, deflection and corresponding load have been recorded with a frequency of 20 Hz. Using each set of specimens at the corresponding temperature, some minutes have been spent between the removal of a broken one and the following because when the climate chamber is opened the temperature inside goes down and so some minutes are necessary to make the temperature homogeneous again. Instead between one set of specimens and the following, at the higher temperature, about two hours have been considered necessary to increase their temperature too.

## 4. Data post-processing

Following the experimental procedure described above a load-displacement curve has been obtained for each specimen at each temperature. Force at the middle section and the run of the middle bearing are directly measured. As we can see in Figure 25, before contact happens, an initial approach movement of the specimen to the middle section bearing is anyway recorded. When the contact starts the recorded force is substantially positive, but the initial phase is mainly characterized by a fluctuant behavior due to the arrangement movements of the specimen on the external support bearings. For each trend the end of this first phase has been detected and chosen as the real begin of the curve and the zero value of the displacement that, from here on, coincides with the deflection of the specimen. Furthermore, the curve shows a very sharp decreasing of load after the peak and a substantially complete sudden loss of mechanical properties. This aspect is typical of a brittle failure behavior of the material and all the data recorded after the peak until the end of the test have been deleted (Figure 26). The curve interval between the peak and the oscillating region is characterized by a quite linear behavior even if some load reductions are present and they can be associated to local incomplete yielding of the material.

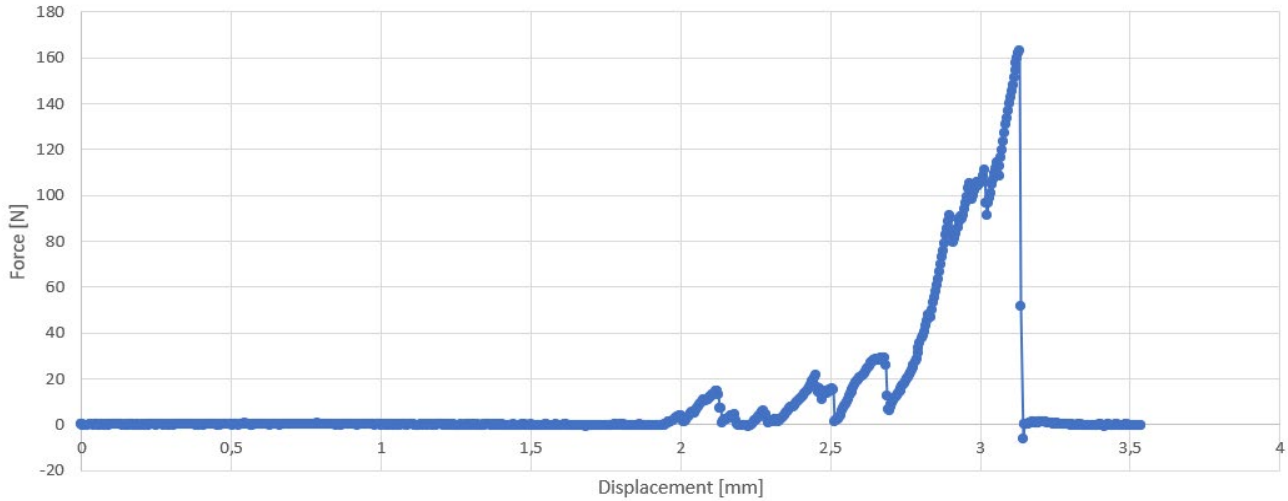


Figure 25: example of load-displacement distribution

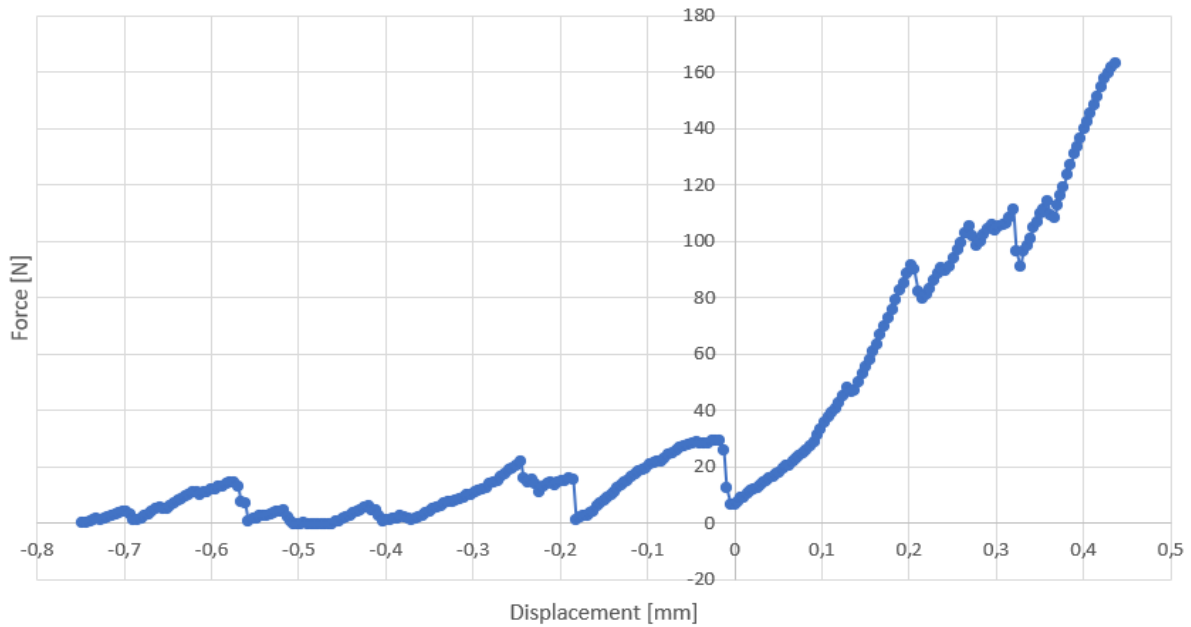


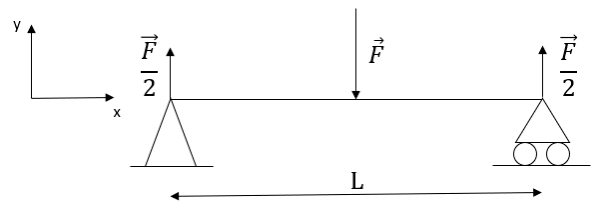
Figure 26

From here on two different approaches have been taken into account in order to get a numerical model able to reproduce structural and mechanical behavior of the sand agglomerated material at the different temperature conditions imposed during tests.

#### 4.1 Approach 1

According to the Euler-Bernoulli beam theory for each coupled data of displacement and associated load a corresponding couple of strain and stress have been computed to build the strain-stress curve. The main hypothesis that characterizes this theory are:

- cross section always perpendicular to the neutral axis.
- effects of shear deformation neglected.
- applicable only for slender beams.



In general, in an isostatic arrangement, stress due to pure bending is:

$$\sigma = \frac{M}{I} \cdot y = \frac{F \cdot x}{2 \cdot I} \cdot y$$

where  $x$  is the distance of a general section from the hinge and  $y$  is the distance from the neutral axis.

Considering the midway section and the rectangular cross section shape the bending stress expression becomes:

$$\sigma = \frac{\frac{F}{2} \cdot \frac{L}{2}}{\frac{b \cdot d^3}{12}} \cdot \frac{d}{2} = \frac{3 \cdot L \cdot F}{2 \cdot b \cdot d^2}$$

The consequent strain expression is:

$$\varepsilon = \frac{6 \cdot b \cdot s}{L^2}$$

where  $s$  is the vertical displacement of the middle section [1].

Through the previous expressions strain and stress have been associated respectively to each couple of data of deformation and load and so graph  $\sigma$ - $\varepsilon$  has been built for each tested specimen.

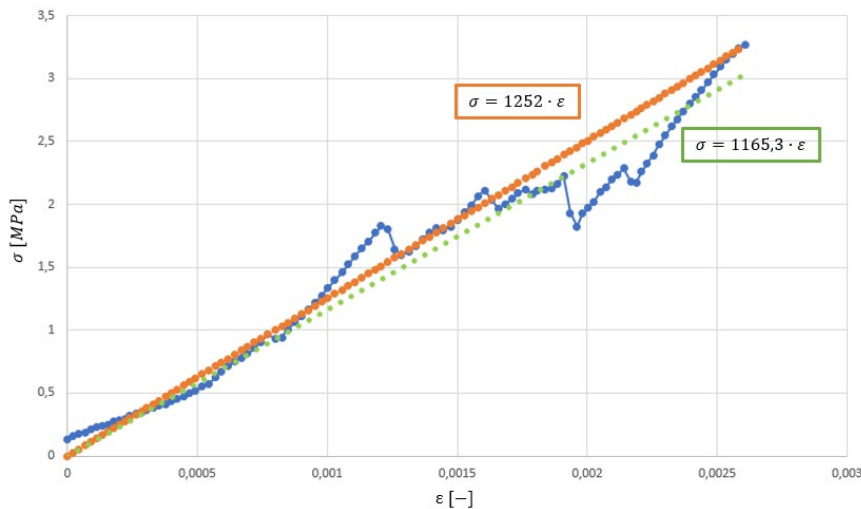
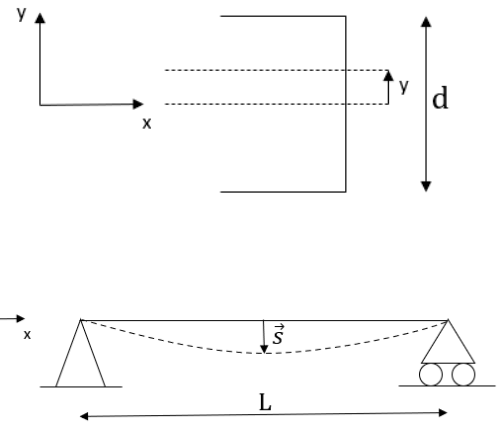


Figure 27: stress-strain curve and linear Young's modulus

As shown in Figure 27, the corresponding Young's modulus has been detected considering a perfectly linear elastic model of the material. Elastic modulus has been defined considering two different possibilities: the slope of the trendline that minimize the root mean square (green) and the slope of the line passing through the origin and the breaking point (orange). So now for each group of specimens that corresponds to the various temperatures there are three or four, only in case of 25 °C, different values of Young's modulus, stress and strain at failure condition. From the collected data it can be noted that increasing the temperature, breaking load decreases while the displacement increases and consequently there is a reduction of the Young's modulus. This aspect is in accordance with the expectation that the material softens increasing the temperature, but this general tendency seems not to be true at 350 °C where a sudden fall of the displacement is recorded while the braking load does not change considerably. As a direct consequence the Young's modulus increases sharply.

Temperature [°C]	Test	s [mm]	F [N]	$\sigma$ [MPa]	$\epsilon$ [-]
25	25_1	0,240	247,67	4,958	0,001436
	25_2	0,361	229,22	4,589	0,002155
	25_3	0,321	214,28	4,290	0,001918
	25_4	0,395	227,04	4,545	0,002362
100	100_1	0,436	163,05	3,264	0,002607
	100_2	0,384	158,10	2,963	0,002276
	100_3	0,350	145,92	2,921	0,002092
200	200_1	0,409	139,67	2,796	0,002444
	200_2	0,442	123,78	2,478	0,002638
	200_3	0,423	132,59	2,654	0,002529
275	275_1	0,383	109,80	2,198	0,002287
	275_2	0,426	114,36	2,289	0,002542
	275_3	0,581	136,05	2,724	0,003473
350	350_1	0,190	103,86	2,079	0,001134
	350_2	0,282	106,83	2,139	0,001684
	350_3	0,200	114,81	2,298	0,001197
480	480_1	0,138	36,91	0,739	0,000827
	480_2	0,294	40,80	0,817	0,001754
	480_3	0,167	41,40	0,829	0,000997

Table 3: values at breaking point for each test

Temperature [°C]	Test	Young's Modulus [MPa]	Young's Modulus [MPa]
25	25_1	3309,0	3452,1
	25_2	1915,1	2129,1
	25_3	1916,1	2236,8
	25_4	1575,6	1924,1
100	100_1	1165,3	1252,0
	100_2	1210,0	1405,0
	100_3	1325,5	1396,6
200	200_1	1003,6	1144,2
	200_2	853,6	939,1
	200_3	879,3	1049,6
275	275_1	871,9	961,0
	275_2	738,7	900,6
	275_3	656,8	784,2
350	350_1	1817,3	1833,1
	350_2	1260,1	1269,8
	350_3	1980,2	1920,8
480	480_1	1052,3	893,2
	480_2	454,8	465,6
	480_3	847,3	831,0

Table 4: Young's modulus considering linear trendline (green) and breaking point intersection line (orange)

The second option (orange) has been chosen as the more appropriate one because the curve has a bumping behavior, with local sharp decreasing of stress, and it can suggest, as we can expect also considering the large variability of the data collected at same temperature, that the mechanical characteristics of a specific specimen are deeply influenced by the microstructure. In fact, the sand mixture is an agglomerate, and the uniformity of the material is not feasible.

#### 4.1.1 Statistical analysis

In brittle materials, as in this case, strength depends on size, position, shape and orientation of defects. Flaws of different nature can derive from manufacturing and machining processes and they are difficult to be removed. Therefore, even in a set of nominally identical specimens, a strength distribution function is required to describe the probability of failure and consequently the reliability. The Weibull distribution function is the most used function for the characterization of brittle materials. According to the “weakest link theory” in brittle agglomerates, fracture originates at defects where stresses are concentrated by the microstructure. A defect is defined as “critical” if stresses in its region are high enough to destroy the cohesion of the material. The minimum size to define a defect as critical depends on several parameters as the type of defect, its shape, its orientation, and the stress state in its region. A procedure of evaluation that considers not only the dependency of failure by the stress state but also by the sample size is necessary. The size effect describes the dependency of mechanical properties by the dimension of the component: as the size of the specimen geometry increases, then, on average, the tensile strength decreases. The reason is that in a wider volume of material the possibility to encounter a critical defect is higher [7]. A series of assumptions have to be considered to derive the probability of failure of brittle material [5]:

- The density of defects is low enough so that the interaction between flaws can be neglected.
- Material fails when the weakest link fails.
- Identical specimens have same density of critical defects.
- All the critical flaws are of one type.

The double parameter Weibull probability density function is:

$$f = \frac{m}{\sigma_{\theta}^m} \cdot \sigma^{m-1} \cdot \exp\left(-\left(\frac{\sigma}{\sigma_{\theta}}\right)^m\right)$$

and the associated probability function is:

$$P_f = 1 - \exp\left[-\left(\frac{\sigma}{\sigma_{\theta}}\right)^m\right]$$

Where:

- $P_f$  is the probability of failure.
- $m$  is the Weibull modulus or shape parameters.
- $\sigma_{\theta}$  is the characteristic strength and it is representative of the test specimen or component.

These two parameters describe respectively the width and the position of the distribution (Figure 28 and 29).

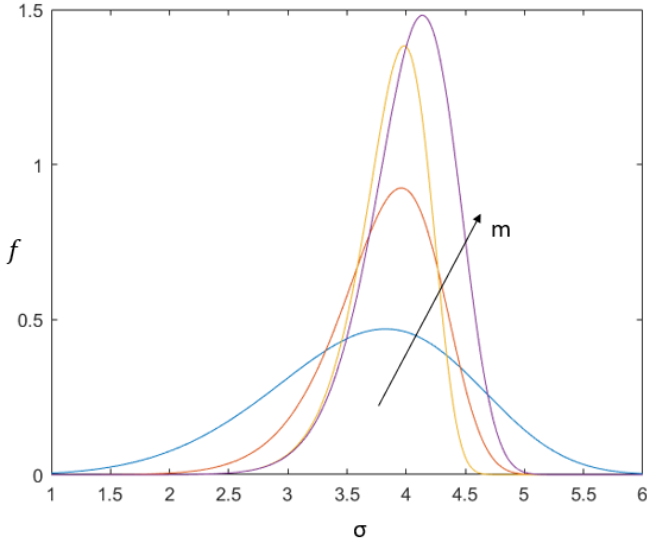


Figure 28: density function

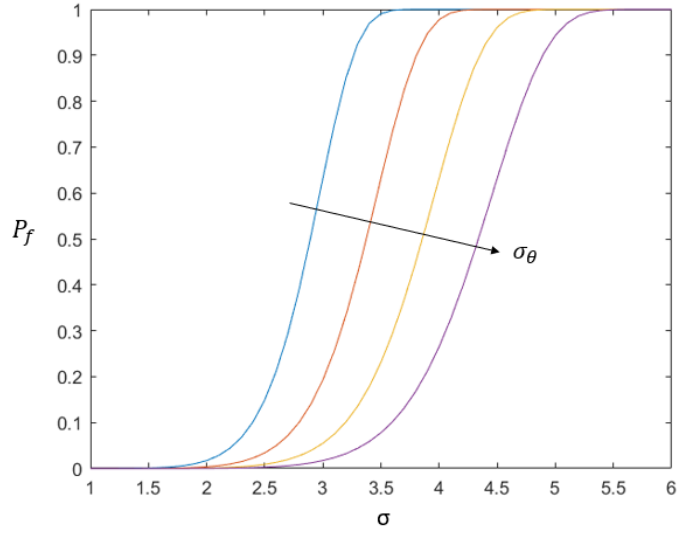


Figure 29: probability function

A more general formulation of the Weibull probability expression, that highlights an inhomogeneous stress state and the presence of a stress gradient in the specimen, is:

$$P_f = 1 - \exp \left[ -V_{eff} \left( \frac{\sigma}{\sigma_0} \right)^m \right]$$

Where:

- $\sigma_0$  is the Weibull scale parameter and it can be described as the Weibull characteristic strength of a specimen with unit volume loaded in uniform uniaxial tension.
- $V_{eff}$  is effective volume that accounts for specimen geometry and stress gradients. In general,  $V_{eff}$  is a function of the estimated Weibull modulus and is always less than or equal to the test specimen volume. The effective volume can be interpreted as the size of an equivalent uniaxial tensile specimen that has the same probability of failure as the test specimen.

By the two previous probability equations, it is possible to deduce that:

$$\sigma_0 = V_{eff}^{\frac{1}{m}} \cdot \sigma_{\theta}$$

In the specific case of 3-point bending test

$$V_{eff} = \frac{L_0 \cdot b \cdot d}{2 \cdot (m + 1)^2}$$

The first step consists in estimating both parameters  $m$  and  $\sigma_{\theta}$  and, according with literature, mainly two different approaches can be used, linear regression method (LR) and maximum likelihood method (ML).

#### Linear regression method

For each temperature condition, stresses evaluated at fracture by the 3 points bending tests have been ranked in an ascendent order:

$$\sigma_1 < \sigma_2 < \dots < \sigma_n$$

$$\sigma_i \text{ with } i = 1, 2, \dots, n$$

where  $n$  is the total number of tested specimens at a certain temperature.

For each  $\sigma_i$  a ranked fracture probability  $P_i$  is defined as:

$$P_i = \frac{i - c}{n - 2c + 1}$$

where  $c$  is the constant probability estimator.

Through the previous equation values of  $P_i$  have been calculated assigning to  $c$  the value of 0.5 and 0. In our case tested specimens are 4 ( $n = 4$ ), only in case of environmental temperature (25 °C), while 3 in all other temperature conditions ( $n = 3$ ).

$P_i (T = 25^\circ\text{C})$	$i = 1$	$i = 2$	$i = 3$	$i = 4$
$c = 0.5$	0.125	0.375	0.625	0.875
$c = 0$	0.2	0.4	0.6	0.8

Table 3: values of constant  $c$  in the case of 4 specimens (25 °C)

$P_i$	$i = 1$	$i = 2$	$i = 3$
$c = 0.5$	0.1667	0.5	0.833
$c = 0$	0.25	0.5	0.75

Table 4: values of constant  $c$  in case of 3 specimens

Now the probability function can be rewritten for each specimen case substituting the corresponding  $P_i$ :

$$P_i = 1 - \exp\left[-\left(\frac{\sigma_i}{\sigma_\theta}\right)^m\right]$$

Manipulating appropriately this equation the following equivalent form can be obtained:

$$\ln\left[\ln\left(\frac{1}{1 - P_i}\right)\right] = m \ln \sigma_i - m \ln \sigma_\theta$$

and it can be interpreted as the equation of a line:

$$y_i = m x_i + \lambda$$

where:

- $y_i = \ln\left[\ln\left(\frac{1}{1 - P_i}\right)\right]$
- $x_i = \ln \sigma_i$
- $m$  is the Weibull modulus and it coincides with the slope coefficient of the line
- $\lambda = -m \ln \sigma_\theta$

Using linear regression expression, the two Weibull parameters are defined for each set of specimens at each temperature [7]:

$$m = \frac{\sum_1^n (x_i \cdot y_i) - \frac{1}{n} \sum_1^n x_i \cdot \sum_1^n y_i}{\sum_1^n (x_i)^2 - \frac{1}{n} (\sum_1^n x_i)^2}$$

$$\lambda = \frac{1}{n} \cdot \left( \sum_1^n y_i - m \cdot \sum_1^n x_i \right)$$

$$\sigma_\theta = \exp\left(-\frac{\lambda}{m}\right)$$

According to literature, for the constant  $c$ , values of 0; 0.3; 0.375 or 0.5 can be assumed but in all this cases a certain underestimation of the probability of failure is done and therefore it leads to a lack of reliability and safety. The two values of constant  $c$  chosen to make this kind of analysis (0 and 0.5) are the most common and  $c=0$  also gives the lower underestimation of  $P_f$  especially if the number of specimens is low as in this case [9].

#### Maximum likelihood method

The second possible method is ML. It provides an alternative way to define the parameters ( $m$  and  $\sigma_\theta$  through two not linear equations:

$$n + m \cdot \sum_1^n \ln(\sigma_i) - n \cdot m \cdot \frac{\sum_1^n [\sigma_i^m \cdot \ln(\sigma_i)]}{\sum_1^n (\sigma_i^m)} = 0$$

$$\sigma_\theta = \left( \frac{\sum_1^n (\sigma_i^m)}{n} \right)^{\frac{1}{m}}$$

The first equation has been solved, through the usage of the `fsolve` MATLAB function, for each temperature to estimate values of  $m$  and then each one has been used to compute the corresponding  $\sigma_\theta$  with the second equation.

```
x0=1; %guessed value for first solution attempt
f=@(m) ...; %definition of function f
m=fsolve(f,x0); % find value of m that makes f null
alfa=...; %(sum_sigma_i/n)
sigma_teta=(1/alfa)^(1/m); %define sigma_teta value
```

According to literature this method is particularly suitable and advantageous with respect to the linear regression method only in case of a great number of specimens [2], anyway it does not avoid the problem of underestimation of the probability of failure [9].

All the three considered options give similar results of parameters  $m$  and  $\sigma_\theta$ . In the Table 5 are reported the values of parameters considering the four specimens at 25 °C:

	$m$	$\sigma_\theta$
LR ( $c=0$ )	13,602	4,742
LR ( $c=0.5$ )	18,802	4,716
ML	19,998	4,711

Table 5: values of Weibull parameters evaluated through three different methods at 25 °C

#### Results

Due to the fact that the number of tested specimens for each temperature is small, LR method is the more suitable. Furthermore, only parameters obtained with  $c=0$ , are used to compute the value of  $\sigma$  at the 50% of probability of failure for each set of specimens:

$$\sigma_{50\%} = \sigma_\theta \cdot \left( \ln \left( \frac{1}{1-0.5} \right)^{\frac{1}{m}} \right)$$

Following the same procedure also the Young's modulus associated to the 50% have been computed:

$T$ [°C]	$\sigma_{50\%}$ [MPa]	$E_{50\%}$ [MPa]
25	4,616	2438,37
100	3,062	1356,89
200	2,652	1049,05
275	2,417	886,10
350	2,179	1679,04
480	0,798	723,12

Table 6: values of  $\sigma$  and  $E$  at the 50% of probability of failure

The corresponding strain and deformation associated at each case are also computed using these equations:

$$\varepsilon_{50\%} = \frac{\sigma_{50\%}}{E_{50\%}} ; s_{50\%} = \frac{\varepsilon_{50\%} \cdot L_0^2}{6 \cdot d} ; F_{50\%} = \frac{2 \cdot b \cdot d^2 \cdot \sigma_{50\%}}{3 \cdot L}$$

$T$ [°C]	$\varepsilon_{50\%}$ [-]	$s_{50\%}$ [mm]	$F_{50\%}$ [N]
25	0,001893	0,317	230,59
100	0,002257	0,378	152,96
200	0,002528	0,423	132,48
275	0,002727	0,457	120,72
350	0,001298	0,217	108,87
480	0,001103	0,185	39,86

Table 7: values of  $\varepsilon$ ,  $s$  and  $F$  at the 50% of probability of failure

#### 4.1.2 Simulation, geometry and settings

The results achieved in previous section are now used to build a 3-point bending simulation. According with the beam theory previously showed a Static-Structural system has been set to create a mono-dimensional isostatic beam model. As first step, the material "sand" has been defined in the "Engineering data" section, assigning to each temperature the corresponding value of Young's modulus and Poisson's coefficient. Material characterization has been performed using the modulus, corresponding to 50% of probability of failure, computed with LR method and  $c=0$ .

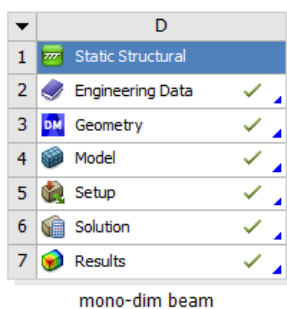


Figure 30: Static-Structural system

Temperature (C)	Young's Modulus (Pa)	Poisson's Ratio
25	2,4384E+09	0,3
100	1,3569E+09	0,3
200	1,049E+09	0,3
275	8,861E+08	0,3
350	1,679E+09	0,3
480	7,2312E+08	0,3

Table 8: Ansys Workbench data table acquisition for material definition and graph

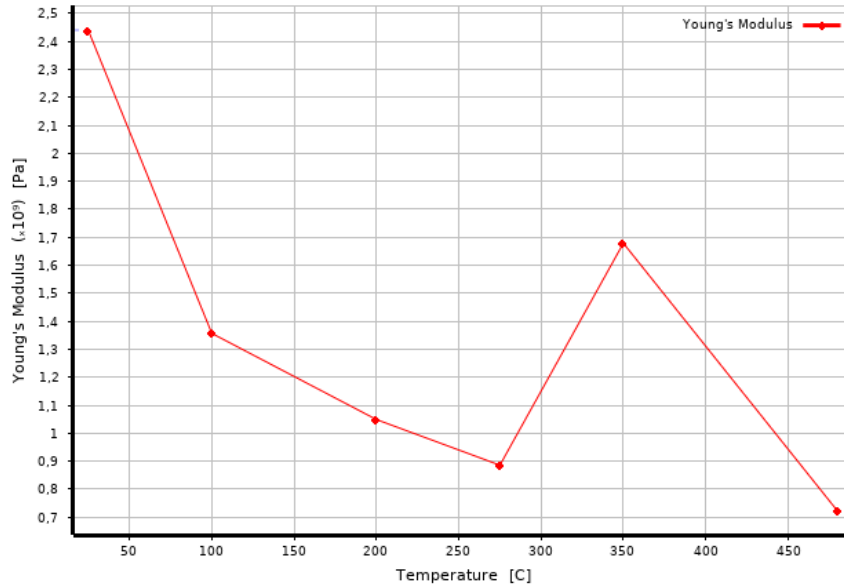


Figure 31: Piece-wise linear definition of Young's modulus as a function of temperature

The software automatically generates a piece-wise linear function (Figure 31) that cover all the temperature range, linking the points defined by the parameters of Table 8. Regarding the Poisson's coefficient, a specific description for core sand agglomerates does not exist in literature and dedicated tests should be necessary to define it experimentally.

The global setting of the Static Structural section (Figure 32 and 33) consists mainly in the definition of a "line body", with length equal to 150 mm, whose cross-section is square shape with the edge 22,4 mm long. The beam has been divided in 1500 divisions through an edge sizing; the hinge-roller constraints have been set at the ends, while the force has been imposed in the midway section. Furthermore, a general thermal condition has been imposed to assign tests temperatures. The aspects evaluated in the solution section are deformation, bending moment and stress and the latter is expected to be equal to the values of  $\sigma_{50\%}$ , previously computed through statistical procedure.

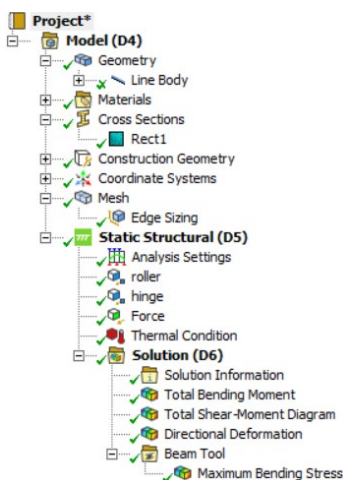


Figure 32: project scheme in Static Structural setup

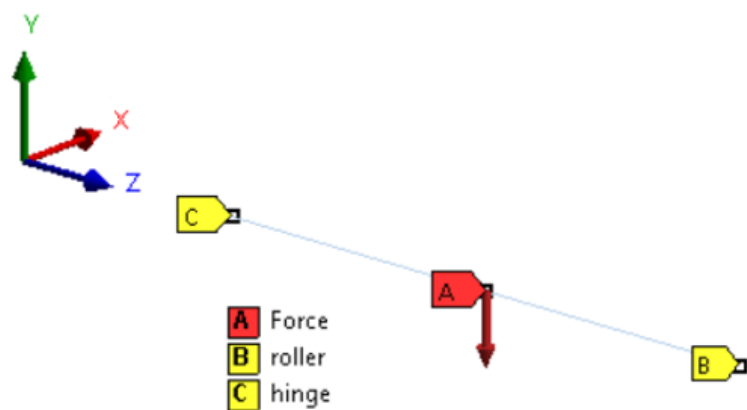


Figure 33: force and constraints sketch

As was expected the values of stress in the middle section coincide with the  $\sigma_{50\%}$  defined before through the Weibull statistical method but the deformation not precisely because this case is not a pure bending condition, a certain

deformation is also due to shear that, in accordance with the Euler-Bernoulli theory, has been neglected. For this reason, the computational results cannot be perfectly coincident with the results got by the simulation.

$T$ [°C]	$F_{50\%}$ [N]
25	230,59
100	152,96
200	132,48
275	120,72
350	108,87
480	39,86

Table 9: load inputs

Deformation [mm]	Bending Moment [N·mm]	Bending stress [MPa]
0,33539	8647,1	4,6161
0,40381	5736	3,0621
0,45237	4968,1	2,6521
0,48802	4527	2,4167
0,23227	4083	2,1794
0,19745	1495	0,79795

Table 10: Results about the middle section

## 4.2 Approach 2

In order to characterize the material, a second possible approach has been taken into account. It has been developed mainly to detect the possible approximations done, considering all the assumptions previously valid. So now the Euler-Bernoulli beam theory is no more exploited, and the idea is to replace that with Timoshenko beam theory. The main hypothesis, considered in the previous approach, now are no more valid:

- the plane sections, perpendicular to the neutral axis before deformation, remains plane but not necessarily perpendicular after deformation
- effects of shear deformation are included
- validity also for short, fat and not only slender beams

### 4.2.1 Simulation

The main difference of this second approach consists in directly exploiting the data of force and deformation, in breaking condition, obtained through the tests. The “Static structural” system is set as the one used in the previous approach but the simulation is now parametric.

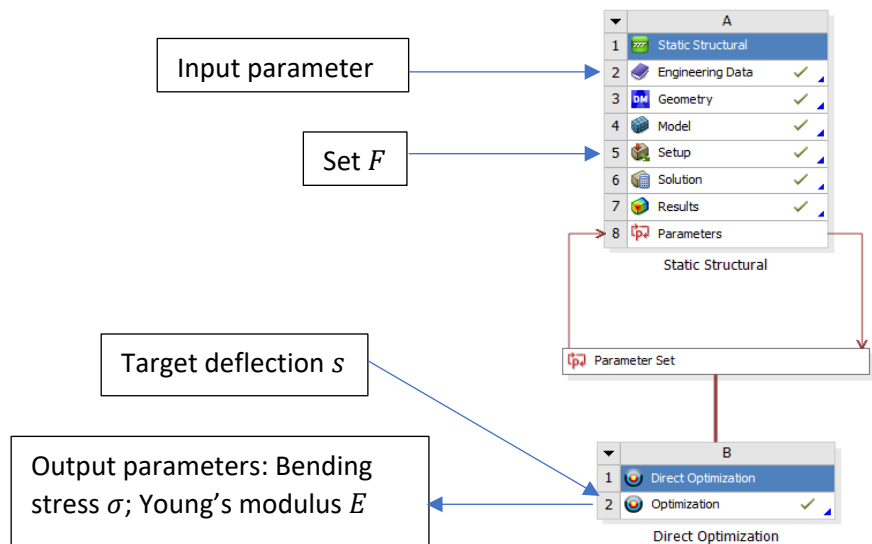


Figure 34: Static structural with optimization

Starting from the setup, already described in Figure 32 and 33, the data value of load associated to each specific tested specimen for each temperature has been inserted as “Force” in the midway section of the beam. Young’s modulus has been defined as a parameter in the “Engineering Data”, while in the “Optimization” section a plausible range of values has been indicated to allow the software to search for the correspondent value inside that. The constraint of deformation too has been inserted as a target value in the “Optimization” section. The software repeats more and more times the bending simulation applying the imposed force and changing at each attempt the

value of the modulus until the target deformation is not obtained. This iterative procedure has been developed for each case at each temperature. Values of stress and modulus are obtained and considering also in this case the hypothesis of perfectly elastic material the strain is computed:

$$\varepsilon = \frac{\sigma}{E}$$

Temperature [°C]	Test	s [mm]	F [N]	$\sigma$ [MPa]	E [MPa]	$\varepsilon$ [-]
25	25_1	0,24044	247,67	4,958	3689,8	0,001344
	25_2	0,36082	229,22	4,589	2275,6	0,002016
	25_3	0,32105	214,28	4,290	2390,8	0,001794
	25_4	0,39546	227,04	4,545	2056,6	0,002210
100	100_1	0,43643	163,05	3,264	1338,3	0,002439
	100_2	0,38442	158,10	2,963	1379,2	0,002148
	100_3	0,35016	145,92	2,921	1492,8	0,001957
200	200_1	0,40911	139,67	2,796	1222,9	0,002286
	200_2	0,44171	123,78	2,478	1003,8	0,002469
	200_3	0,42338	132,59	2,654	1121,8	0,002366
275	275_1	0,38290	109,80	2,198	1027,2	0,002140
	275_2	0,42556	114,36	2,289	962,6	0,002378
	275_3	0,58142	136,05	2,724	838,2	0,003249
350	350_1	0,18988	103,86	2,079	1959,3	0,001061
	350_2	0,28197	106,83	2,139	1357,2	0,001576
	350_3	0,20031	114,81	2,298	2053,0	0,001119
480	480_1	0,13848	36,91	0,739	954,7	0,000774
	480_2	0,29366	40,80	0,817	497,6	0,001641
	480_3	0,16699	41,40	0,829	888,2	0,000933

Table 11: results from approach 2

#### 4.2.2 Statistical analysis

Also in this second case a statistical interpretation of the results listed before has been performed using the Weibull distribution function. Following the same steps as before the  $\sigma_{50\%}$ ,  $\varepsilon_{50\%}$  and  $E_{50\%}$  have been computed. Linear regression method with constant  $c = 0$  has been chosen also in this case.

T [°C]	$\sigma_{50\%}$ [MPa]	$E_{50\%}$ [MPa]	$\varepsilon_{50\%}$ [-]
25	4,616	2497,5	0,001848
100	3,062	1397,1	0,002192
200	2,652	1114,5	0,002380
275	2,417	931,5	0,002594
350	2,179	1735,2	0,001256
480	0,798	729,7	0,001094

Table 12: stress, strain and Young's modulus by Weibull

As expected, results of modulus are generally higher than previous analysis in fact same data values of load and deflection have been used but in this second approach also shear deformation has been considered through the direct computation performed by the software. Therefore an increased stiffness is a natural consequence.

### Poisson coefficient

Since that precise information is not available regarding Poisson's coefficient dependency on temperature and its influence on mechanical characteristics for sand core agglomerates, some brief simulations have been done just changing the value of the coefficient in a plausible range for this kind of material. This kind of analysis considers only the two extreme temperature cases (25 °C and 480 °C).

Poisson ratio [-]	0,1	0,3
	Young's modulus [MPa]	Young's modulus [MPa]
25_1	3653,3	3689,8
25_2	2253,1	2275,6
25_3	2367,1	2390,8
25_4	2036,2	2056,6

Table 13: results at 25 °C of Young's modulus for different values of Poisson's coefficient

Poisson ratio [-]	0,1	0,3
	Young's modulus [MPa]	Young's modulus [MPa]
480_1	945,3	954,7
480_2	492,8	497,6
480_3	879,3	888,2

Table 14: results at 480 °C of Young's modulus for different values of Poisson's coefficient

As showed in Table 14 and 15 modulus is only slightly influenced by the Poisson's ratio both in case of high and low temperatures, so the value of 0.3 has been chosen as the one used for the simulations.

### 4.3 Friction effect error in flexural testing

A possible error can be introduced due to the presence of frictional forces between the test-piece and the bearings. The arc length of the test-piece increases because of the elastic strain and tends to push outwards on the supports. If the rollers, supporting the test piece, are not free to roll to accommodate this change, a lateral frictional force is developed at the contact points which is proportional to the applied force [8].

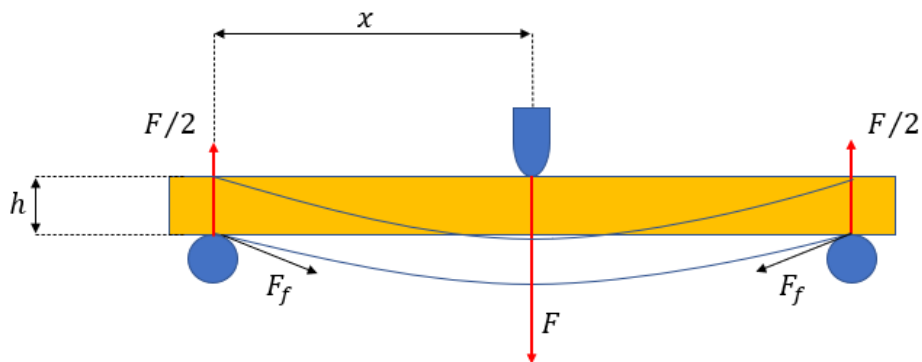


Figure 35: 3-point bending scheme with friction force

If the effect of frictional force is considered the equivalent bending moment is:

$$M = \left(\frac{F}{2} \cdot x\right) - M_f = \left(\frac{F}{2} \cdot x\right) - (F_f \cdot h) = \left(\frac{F}{2} \cdot x\right) - \left(\frac{F}{2} \cdot \mu \cdot h\right) = \frac{F}{2} \cdot (x - \mu \cdot h)$$

A typical value of the friction coefficient  $\mu$  for a contact with unlubricated metal is 0.3. Considering this additional term in the moment expression the percentage error committed on the stress can be computed through:

$$e = 100 \times \left( \frac{\mu}{\frac{x}{h} - \mu} \right)$$

In this case considering the loading arm for the mid span section  $\frac{150 \text{ mm}}{2} = 75 \text{ mm}$  and  $h = 22.4 \text{ mm}$  the estimated error on stress is about 10%.

Simulations of 3-point bending have been performed considering frictional contacts between the sand bar and the bearings. Stress values have been computed following again the iterative and optimization procedure. Values of deformation and force have been directly exploited again to evaluate stress, strain and Young's modulus according to the scheme of Figure 34. For these simulations whole 3D geometry has been set: frictional contacts have been set with a friction coefficient equal to 0.3; load has been imposed on the upper surface of the mid bearing while the lower surfaces of the external bearings have been set as fixed supports (Figure 35); targeted deflection has been imposed to the load bearing (Figure 36) in the "Optimization" section and a probe has been located in the center of the lower face of the bar.

Specimen	Load [N]	Deflection [mm]	$E$ [MPa]	$\sigma$ [MPa]	$\sigma_{10\%}$ [MPa]
25_1	247,67	0,24044	3528,0	4,493	4,462
25_2	229,22	0,36082	2175,2	4,157	4,130
25_3	214,28	0,32105	2285,5	3,886	3,861
25_4	227,04	0,39546	1965,6	4,118	4,091

Table 15: simulation data and results

In Table 16, regarding the four specimens at room temperature,  $\sigma$  is the value of stress in the probe location, while  $\sigma_{10\%}$  is the value of stress obtained reducing of 10% values of Table 11. It considers the error due to the presence of friction. The obtained values of  $\sigma$  are very similar to the estimated values of  $\sigma_{10\%}$  and they do not differ by more than 1% for all four cases.

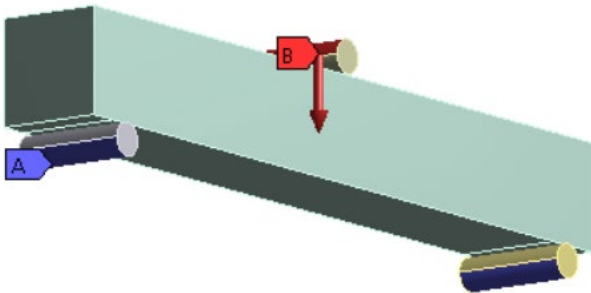


Figure 36: fixed supports and load

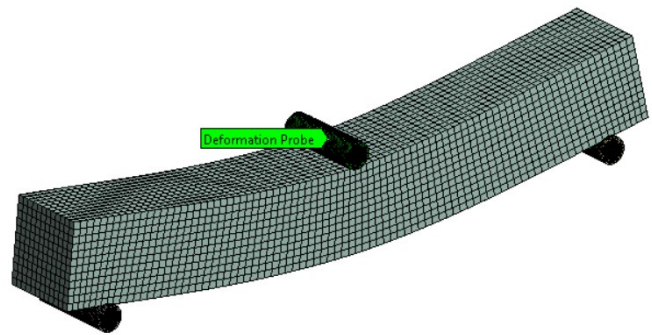


Figure 37: deformation probe

Through the following series of simulations, the pouring of the molten aluminum has been characterized with particular attention to all the possible aspects of the interaction between the fluid metal and the solid sand core. All simulations are built in Ansys Workbench in accordance with Figure 38. The results of interest obtained in the "Fluent" section are used as input for the "Static Structural".



Figure 38: General scheme of metal-static simulation

## 5. METAL-STATIC SIMULATION

### 5.1 Fluent geometry

The geometry of Figure 39 represents the shape of the cavity in the steel die that is filled with molten metal. The ends of the bar are locked in two cavities obtained in the die. The geometry is characterized by:

- a conical shape where the molten metal is poured from the crucible
- a channel to lead metal to the double narrow inlets
- a stepped structure where sand bar is located

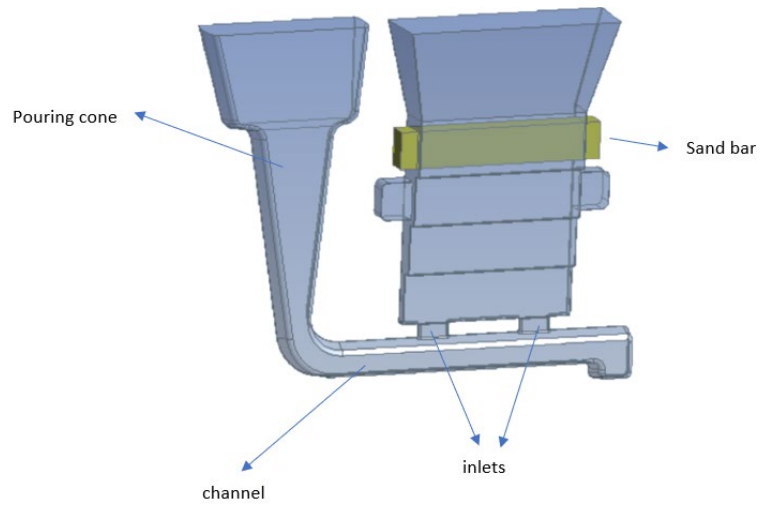


Figure 39: Shape of cavity in the die and sand

### 5.2 Fluent setup

The setup is characterized by the definition of the density of molten aluminum that generates a pressure gradient on the bar (Figure 40).

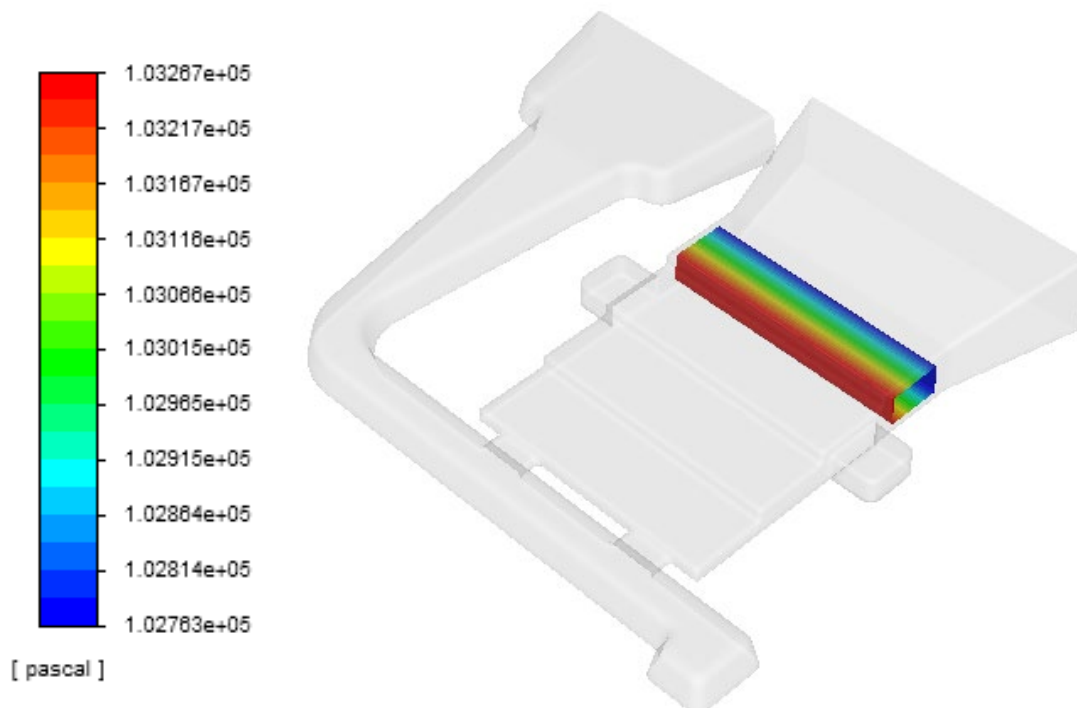


Figure 40: pressure gradient on the bar-aluminum

Considering the density of the molten metal and the immersed volume, so the entire volume of the bar just excluding the two sides locked in the steel die, a preliminary analytical computation of the buoyancy force can be performed:

$$F = \rho_{al} \cdot V_{sub} \cdot g = 0.655 \text{ N}$$

where:

- $V_{sub} = 28653 \text{ mm}^3 = 2.8653 \cdot 10^{-5} \text{ m}^3$
- $\rho_{al} = 2330 \frac{\text{kg}}{\text{m}^3}$

The force is along Z axis in negative direction.

### 5.3 Fluent results

In the “Results” section, fluid dynamic results from “Fluent” have been analyzed and the force applied on each of the four faces of the bar have been obtained separately. Values of perpendicular forces have been derived from integrals of static pressure on the respective surface:

- On the superior surface the force is Z positive directed and equal to  $F_{sup} = 1.874 \text{ [N]}$
- On both lateral surfaces the force is almost same and equal to  $3.8 \text{ [N]}$
- On the inferior surface the force is Z negative directed and equal to  $F_{inf} = 2.529 \text{ [N]}$

So, the resultant force along Z is:

$$F_{sup} - F_{inf} = -0.655 \text{ N}$$

Completely in accordance with the value computed analytically.

### 5.4 Static Structural

The force computed generates a consequential deformation of the sand bar. In the “Static Structural” section this deformation has been evaluated applying the pressure field as an external load. The geometry for this section is simplified (Figure 41): only half of the bar is considered, exploiting symmetry, and the steel fixed support replaces the entire die.

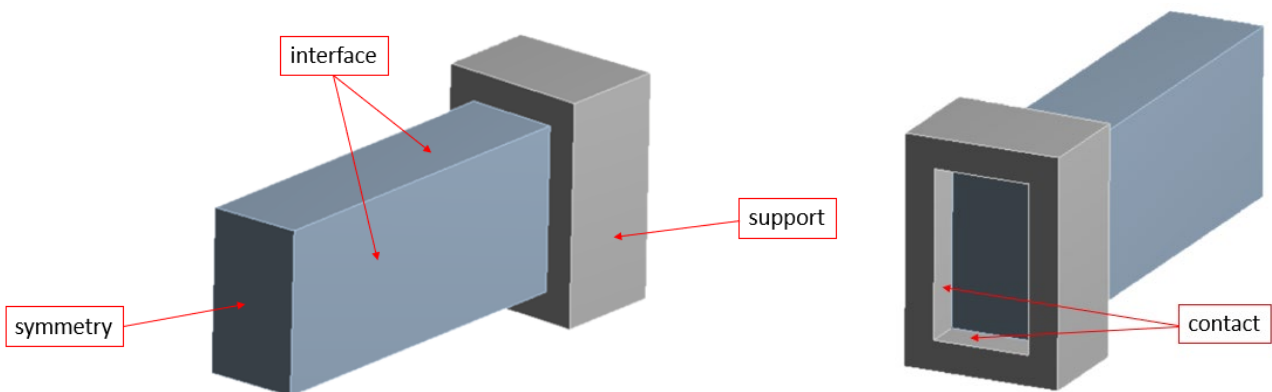


Figure 41

Imposing the support external faces as fixed, considering the earth gravity and the contact between the bar and the support as frictionless, Z directional deformation (Figure 42) is computed in correspondence of the probe located in the center of the lower edge on the symmetry face (Figure 43):

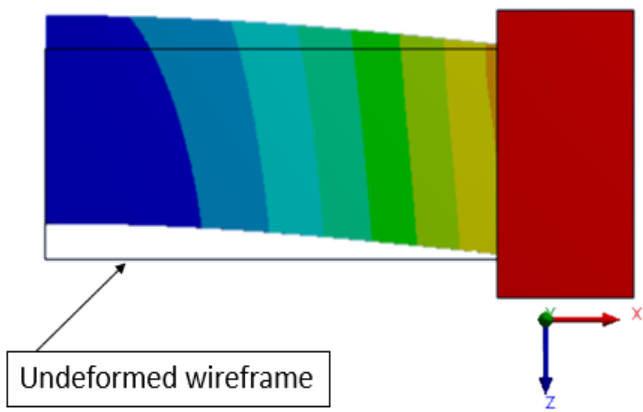


Figure 42: deformation field (Z direction)

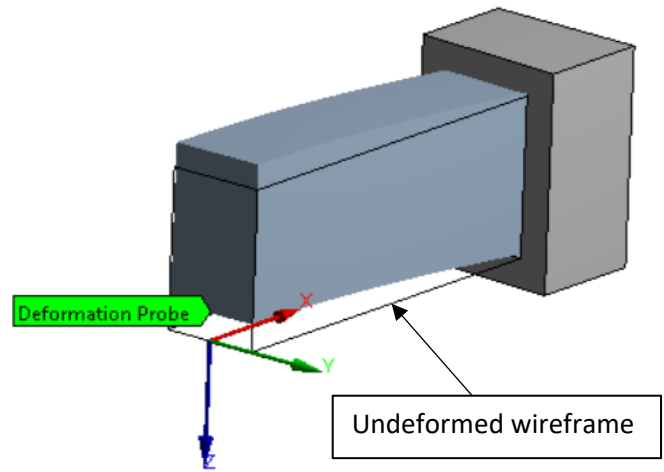


Figure 43: deformation probe location

Maximum deformation is in the symmetry middle section, as expected, and equal to:

$$1.127 \cdot 10^{-4} [mm]$$

This value of deformation is obtained considering the mechanical characteristics of the sand material, assigned to the bar, as it is at environmental temperature. This result can be considered suitable just for a certain time after the complete filling of the die when the molten aluminum is rest and the temperature is increased just in the superficial layer of the bar and so the mechanical characteristics are not deeply modified.

## 6. DYNAMIC-METAL FORCE SIMULATION

### 6.1 Fluent geometry

In this simulation the considered geometry is derived removing not necessary parts and exploiting again symmetry to reduce as much as possible the complexity and consequently the computational effort. Figure 44 shows the geometry that is obtained cutting the same geometry of previous simulation with YZ plane and another parallel to XY and some millimeters below the bar.

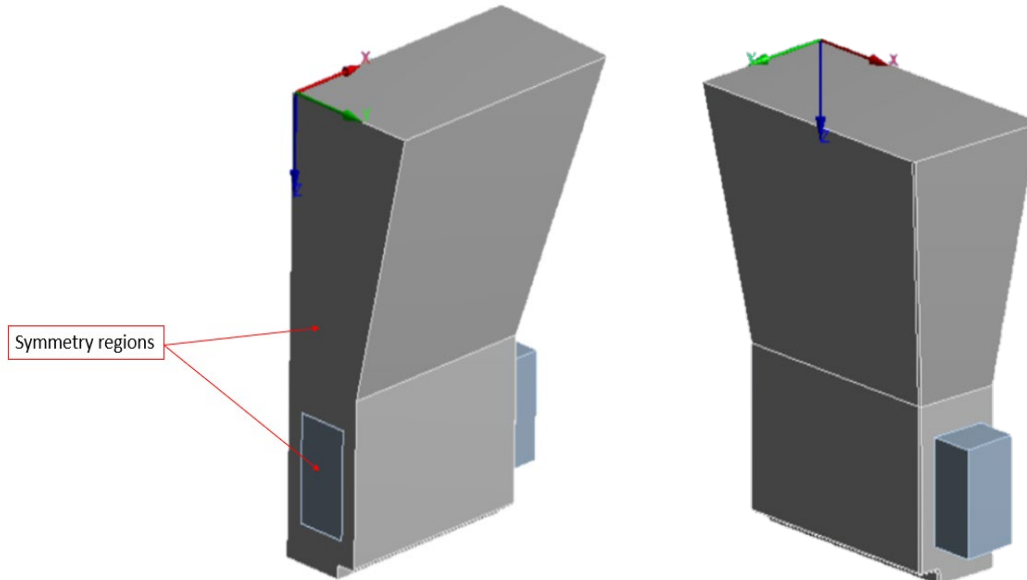


Figure 44

### 6.2 Fluent setup

The general scheme is the same of the previous simulation but there are deep differences in “Fluent” section: here a multiphase VOF model is necessary (Figure 45) and molten aluminum (red) enters in control volume with a certain mass flow rate from the lower surface, pushing out the air (blue) from the upper one.

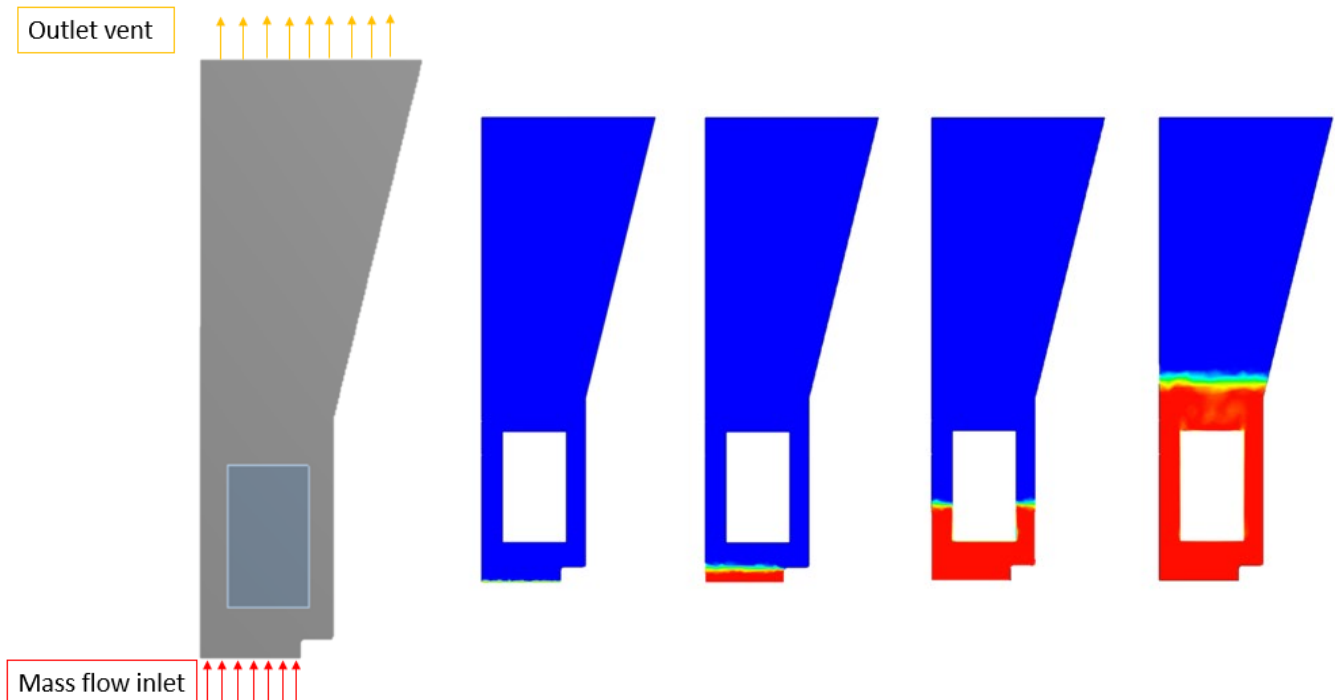


Figure 45: fluid domain filling and boundary conditions

Considering a filling period of the entire fluid domain of about 3 seconds the mass flow at the inlet has been computed:

- Volume of fluid domain  $V = 116799 \text{ mm}^3$ ;
- Area of inlet surface  $A_{in} = 822.5 \text{ mm}^2$ ;
- Filling time  $t = 3.1 \text{ s}$ ;

Volumetric flow rate:

$$\dot{V} = \frac{V}{t} = 37677 \frac{\text{mm}^3}{\text{s}}$$

Mass flow rate:

$$\dot{m} = \rho \cdot A_{in} \cdot v = \rho \cdot \dot{V} = 0.0877 \frac{\text{kg}}{\text{s}}$$

### 6.3 Fluent results

Proceeding in the same way of the previous simulation, in the section “Results”, the trends of the forces on each surface of the bar at the interface with the molten aluminum have been computed and analyzed (Figure 46 and 47).

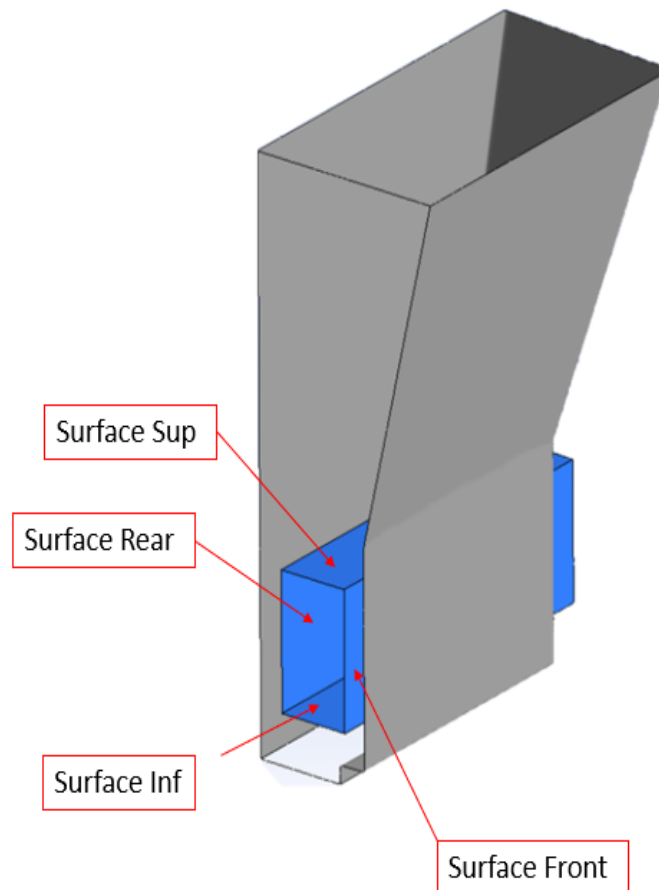


Figure 46

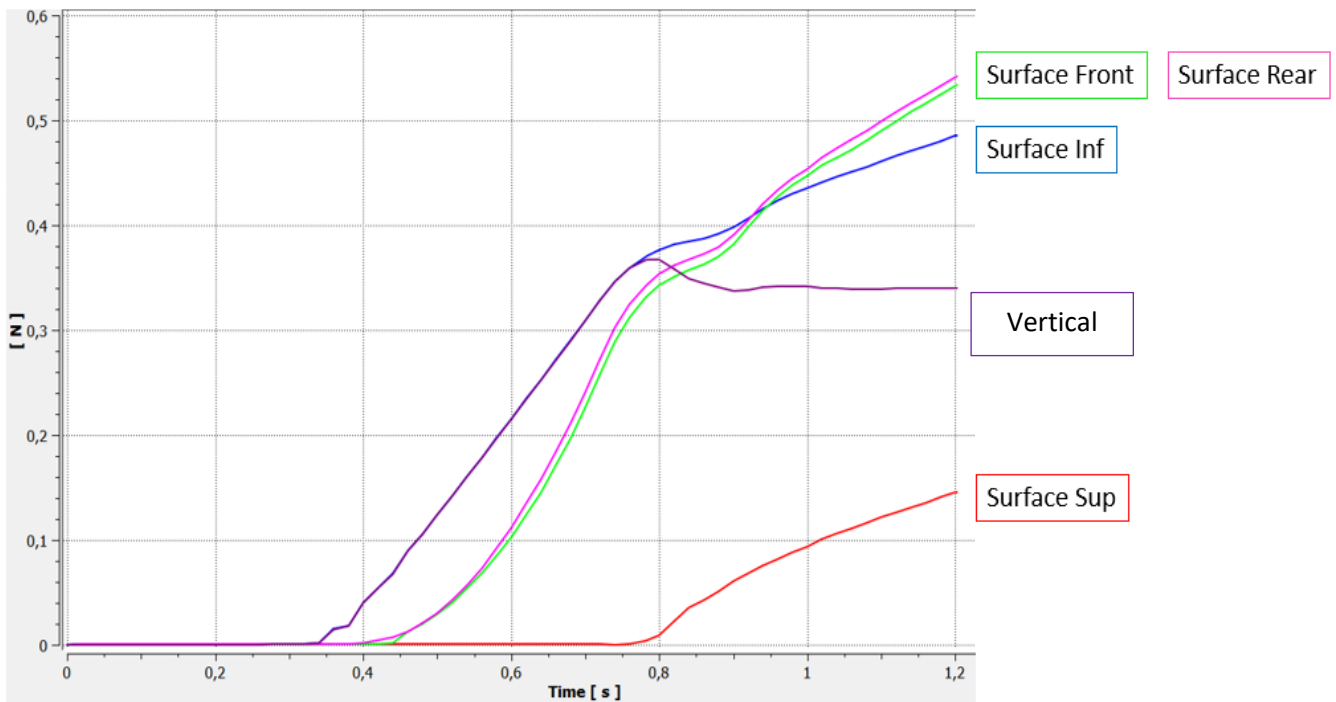
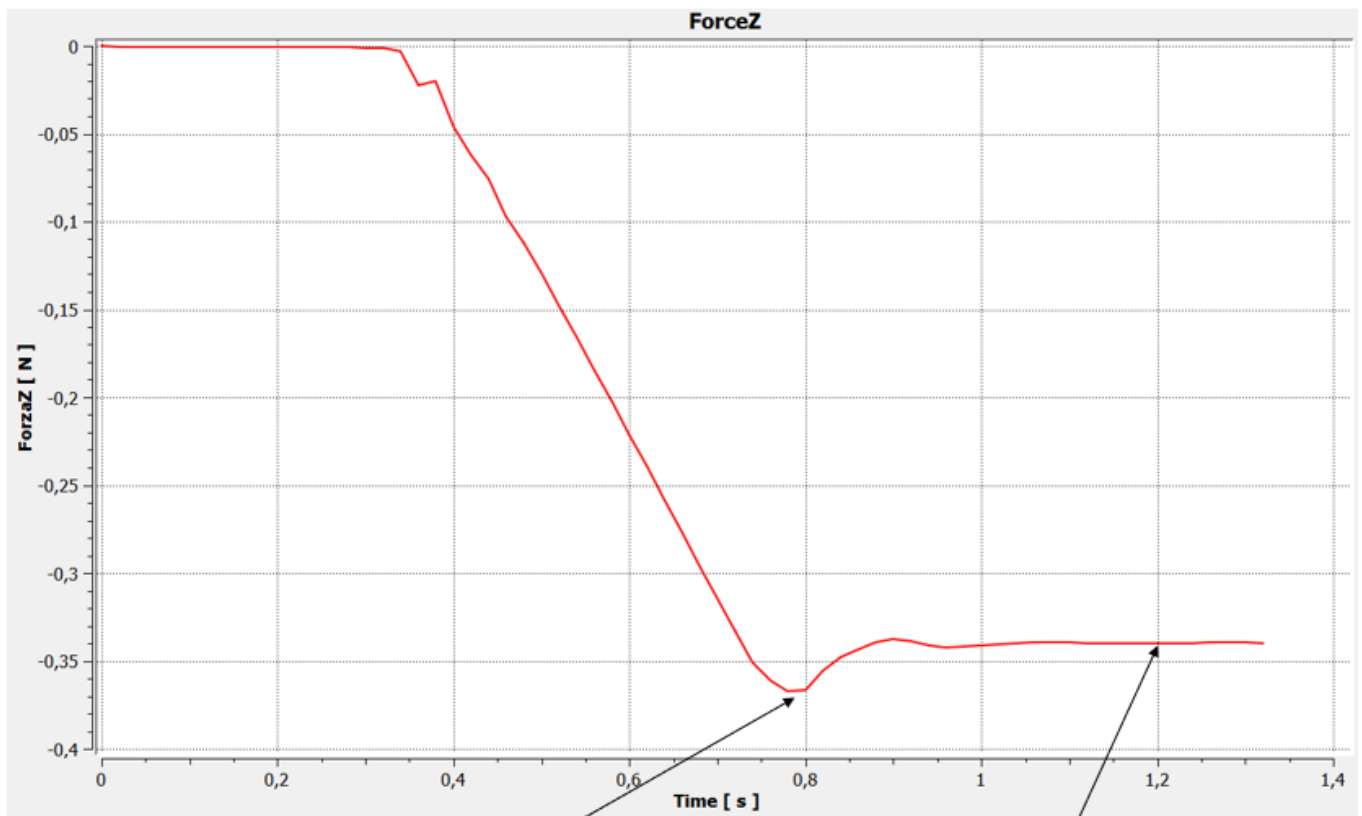


Figure 47

Figure 47 shows the trends of forces. As expected, the forces on the front and rear surfaces are almost the same while the force on the upper surface (red) is null until the flux of aluminum doesn't overcome completely the bar. The vertical force (purple) is computed as the difference between the force on the inferior and superior surfaces.

In Figure 48 the vertical force is represented with the sign in accordance with the frame of reference. In the instant that fluid aluminum alloy reaches the lower surface of the bar the force, due to the generated pressure field, is no more null. Two specific instants are remarked:

- at 0.78 s the vertical force reaches the maximum value because submerged volume is the maximum, while after that the force on the upper surface starts to partially counterbalance the force on the lower part.
- at 1.2 s the vertical thrust is already almost constant because the bar is completely submerged so the buoyancy force is constant.



Time [s]	0,78
Force Z [N]	-0,36731

Time [s]	1,2
Force Z [N]	-0,34008

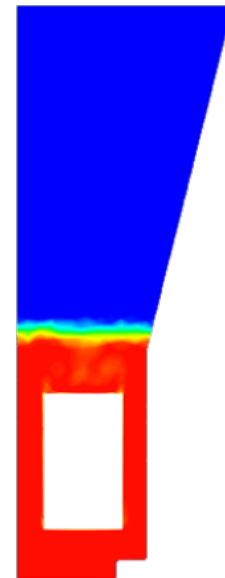
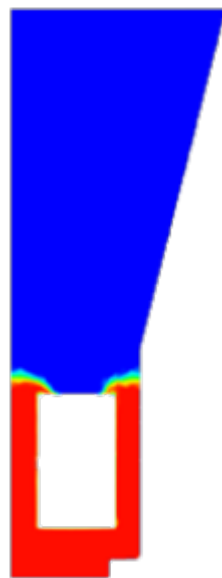


Figure 48: Evolution of force in z-direction

Forces computed in dynamic case apparently seem smaller than the one in static case but for this simulation the symmetry, with respect to XY plane exploited, halves the surface of the interface between the bar and the fluid and the force is computed as the integral of pressure on the area. The values obtained must be doubled to make them comparable with the result of static case. The resultant force of the constant region depends on both buoyancy and drag effects.

## 6.4 Static Structural

The load trend obtained has been used in the “Static Structural” section to develop the evolution of deformation in vertical direction. Here again the simplified geometry constituted by a half of the bar, thanks to symmetry, and the support, that substitutes the entire steel die, has been used. Deformation is again evaluated in a probe located as shown for the static case. Figure 49 shows the trend, and the same instants are remarked. It is possible to detect the instant of the arrive of the molten metal, in fact the deformation is initially constant and positive due to the weight force, and from that instant on, deformation begins to decrease, reaching the minimum in correspondence of the maximum force. As in the trend of force also the vertical deformation develops quite constantly when the bar is completely submerged.

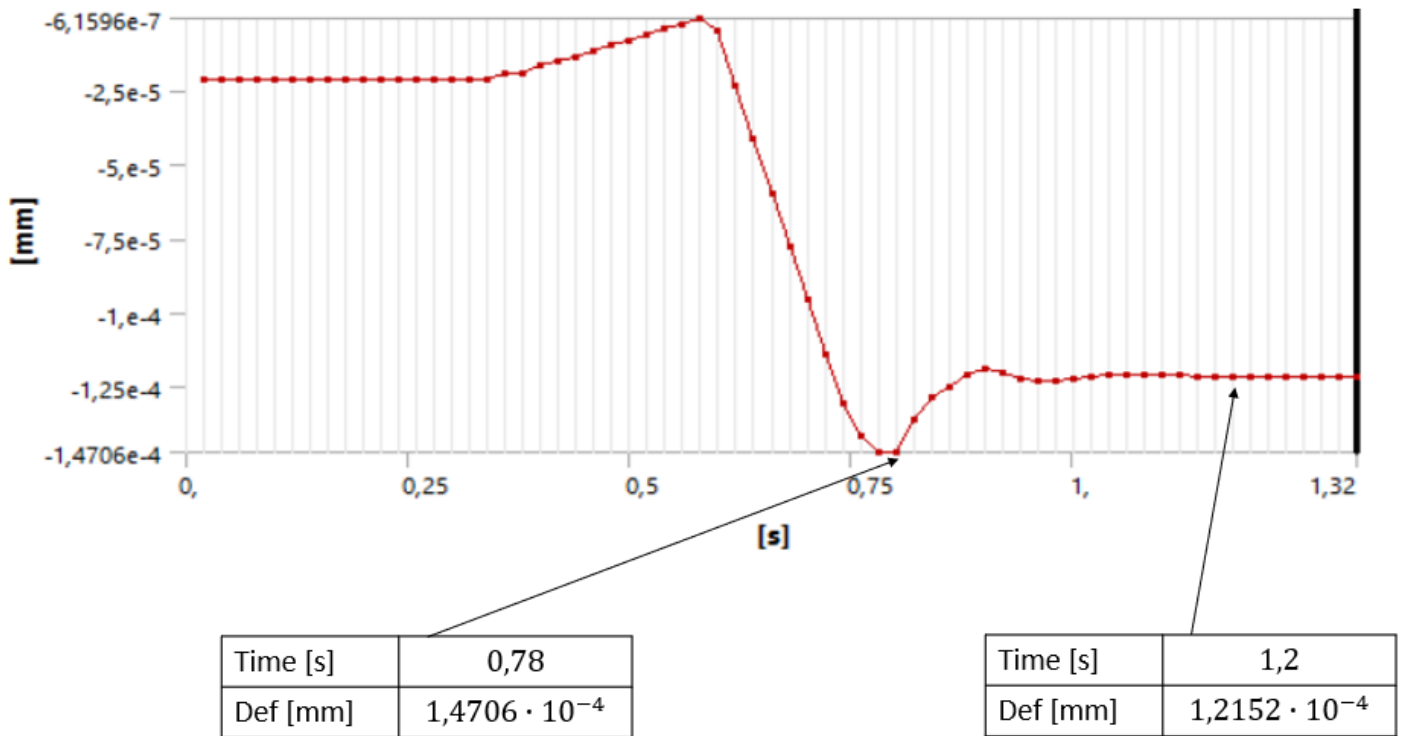


Figure 49: vertical displacement trend

Through this simulation it is possible to understand which is the most critical instant for the bar during the filling process of the die. Here again the mechanical characteristics of the sand are considered as it is at environmental temperature because the bar is relatively cold before the contact with the molten metal.

## 7. SOLIDIFICATION SIMULATION

With this last simulation the objective is to model the molten aluminum alloy behavior during its solidification in the mold and the consequent effect that heat exchanges, phase change and generated pressure have on the sand bar core. The general structure of the Workbench project is the same of Figure 38. In permanent die casting the inner surfaces of the metal mold is painted with a refractory-based powder coating whose principal functions are:

- Control of the metal flow to ensure that it reaches all parts of the die at a sufficient temperature to prevent the formation of seams or cold laps
- Control of heat transfer to obtain better solidification and ensure that the castings are properly fed
- Easy release: since castings are extracted at just below the solidification temperature, easy release ensures that castings do not come out deformed
- Good surfaces, and therefore a reduction in finishing costs
- Longer die life, therefore increased productivity and reduced maintenance

### 7.1 Fluent geometry

Geometry should be constituted by the steel die, the fluid volume of the cavity in the die filled with molten aluminum alloy, the sand core bar locked in the appropriate slots in the mold and a volume of air in touch with the two free surface regions of the molten metal and with the upper surface of the mold (Figure 50).

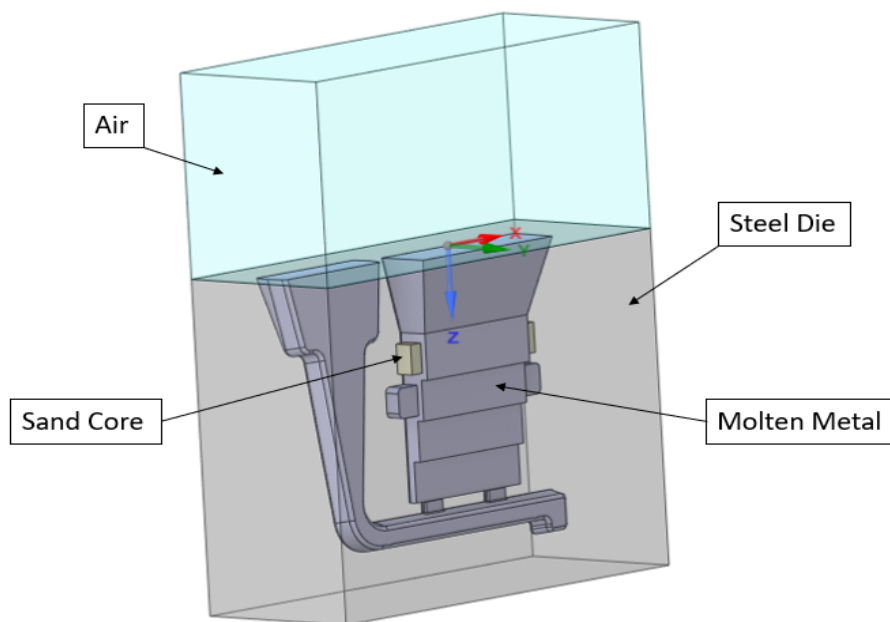


Figure 50

Since it was necessary to reduce the computational effort, a reduced geometry has been considered. Geometry of Figure 50 has been cut by the YZ plane and only the X-coordinate positive region has been used for the simulation. This volume reduction was necessary even if the obtained geometry cannot be considered as a result of symmetry but it has considered a fair compromise to reduce simulation complexity.

## 7.2 Materials

Materials are defined in the “Fluent-Setup” section, air and sand are the same described in 2.3, while steel and aluminum alloy are characterized here below.

### Steel

The thermal characteristics of the steel mold have been defined taking as a reference the one of the AISI H13 that is commonly used in mold manufacturing dedicated to aluminum casting. Since the die is defined as a solid the only needed constant thermal characteristics are:

- Thermal conductivity  $29 \text{ W/m} \cdot \text{K}$
- Specific heat capacity  $470 \text{ J/kg} \cdot \text{K}$

### Coating

The coating paint has been considered as a layer of constant thickness of  $15 \mu\text{m}$  with a thermal conductivity of  $0.152 \text{ W/m} \cdot \text{K}$

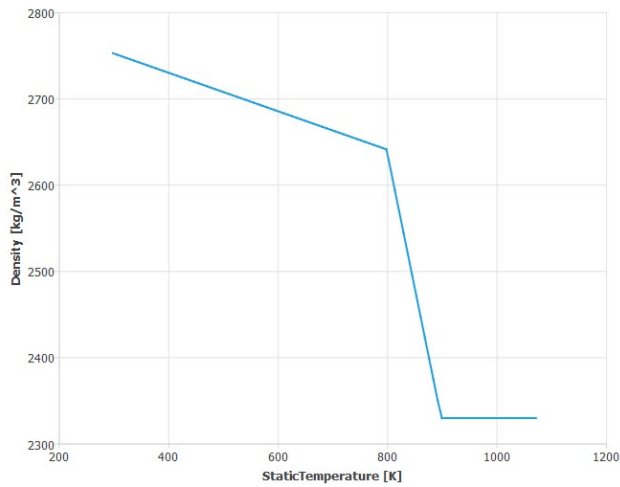
### Aluminum alloy

The aluminum alloy is AISi7Cu3 and all its characteristics has been defined based on a similar alloy AISi5Cu3 whose thermal dependent characteristics are deeply described in [12]. Figure 51 shows all the necessary inputs requested by the software for a material that, as in this case, undergoes a solidification process.

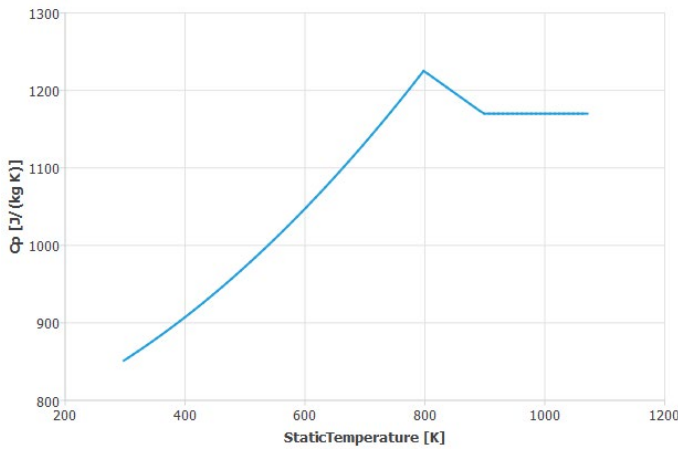
Density [kg/m <sup>3</sup> ]	piecewise-linear	Edit...
Cp (Specific Heat) [J/(kg K)]	piecewise-polynomial	Edit...
Thermal Conductivity [W/(m K)]	piecewise-polynomial	Edit...
Viscosity [kg/(m s)]	constant	Edit...
	0.0013	
Molecular Weight [kg/kmol]	constant	Edit...
	26.9815	
Standard State Enthalpy [J/kgmol]	constant	Edit...
	3.2971e+08	
Reference Temperature [K]	constant	Edit...
	298	
Pure Solvent Melting Heat [J/kg]	constant	Edit...
	390000	
Solidus Temperature [K]	constant	Edit...
	798	
Liquidus Temperature [K]	constant	Edit...
	898	

Figure 51

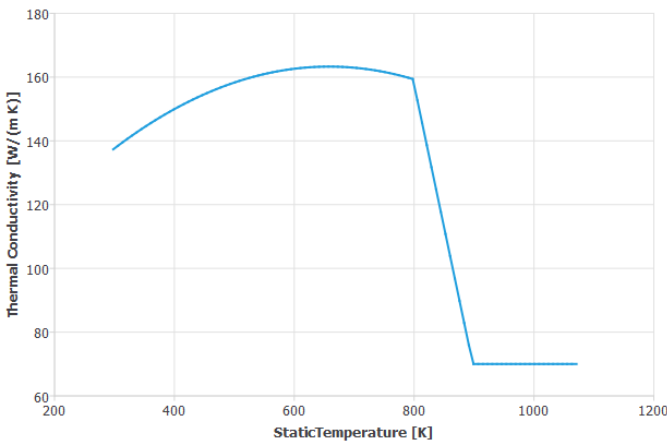
Density, specific heat capacity and thermal conductivity are defined as piece-wise linear or piece-wise polynomial temperature dependent functions.



T [K]	$\rho$ [kg/m <sup>3</sup> ]
298	2753
798	2641.5
898	2330
1071	2330



T range [K]	Cp equation [J/(kg K)]
298 - 798	$0.0005T^2 + 0.2T + 747.3$
798 - 898	$-0.55302T + 1666.612$
898 - 1071	1170



T range [K]	Th cond equation [W/(m K)]
298 - 798	$-0.0002T^2 + 0.2633T + 76.64$
798 - 898	$-0.893926T + 872.7455$
898 - 1071	70

Table 16: temperature dependent characteristics of aluminum alloy

Figure 52: plots of aluminum alloy characteristics

### 7.3 Setup

For this simulation the “VOF” and “Solidification & Melting” models are both activated contemporarily. “VOF” is necessary because in this case two fluids are present in the control volume: air and molten metal, instead “Solidification & Melting” gives the possibility to set solidus and liquidus temperatures to define a range in which both phases coexist, and the liquid fraction quantifies the reciprocal quantity of each. Both air and metal regions are considered as a single fluid part so that a conformal mesh is built at the interface in correspondence of the free surface.

### 7.3.1 Initial condition

The simulated process begins with the molten metal volume filled completely with the phase “aluminum” and the overlying volume with phase “air”. The fluid metal is stationary so this initial condition should represent the start of the solidification after the pouring in the die. Each region is initialized with a temperature:

- Molten aluminum region has an initial temperature equal to 898.1 K, just above the liquidus temperature of the alloy to assure that no solidified regions are already present.
- The steel die is preheated in an oven before starting the pouring process to limit the temperature gradients and the solidification rate, so the initial temperature is set equal to 498 K.
- The sand bar is inserted in the mold after its heating at environmental temperature, so its initial temperature is at 303 K.
- Air temperature is not set constant because of convergence issues and so a variable custom field function is created, temperature changes linearly. Temperature decreases from 898.1 K, just above the free surface, to 498 K at the top. A so high minimum temperature has been considered necessary to avoid the presence of great thermal gradients that should make the simulation unstable especially at the beginning.

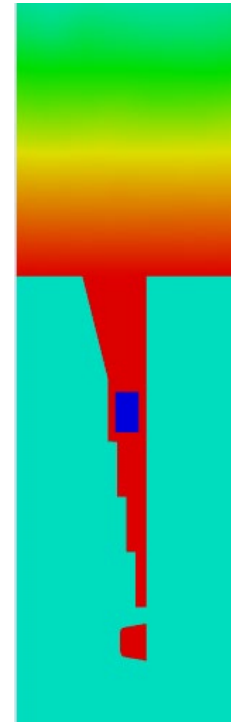


Figure 53: initial temperature field on cross-section

### 7.3.2 Boundary condition

As previously described in section 7.1 the considered control volume consists only in the positive x-coordinate region of the whole geometry. To satisfy the need to reduce the computational effort this reduced geometry with symmetry regions on both fluid zones has been considered a fair compromise. The external walls of the die are considered simply adiabatic because the thermal inertia of the die is high enough to avoid a consistent increase in temperature of these walls during the solidification period. In addition to the symmetry, the boundaries of the air regions are three lateral walls, that don't allow air to pass through, and a top outlet that guarantees both entrance and exit of fluid. The choice of not permeable lateral walls is necessary to avoid convergence issues and solution instability, giving air the only chance to exit and enter from the top, consequently simplifying the management of the air motion. All the interfaces between molten metal and steel die are defined as “coupled” to set the coating layer described in section 7.2.

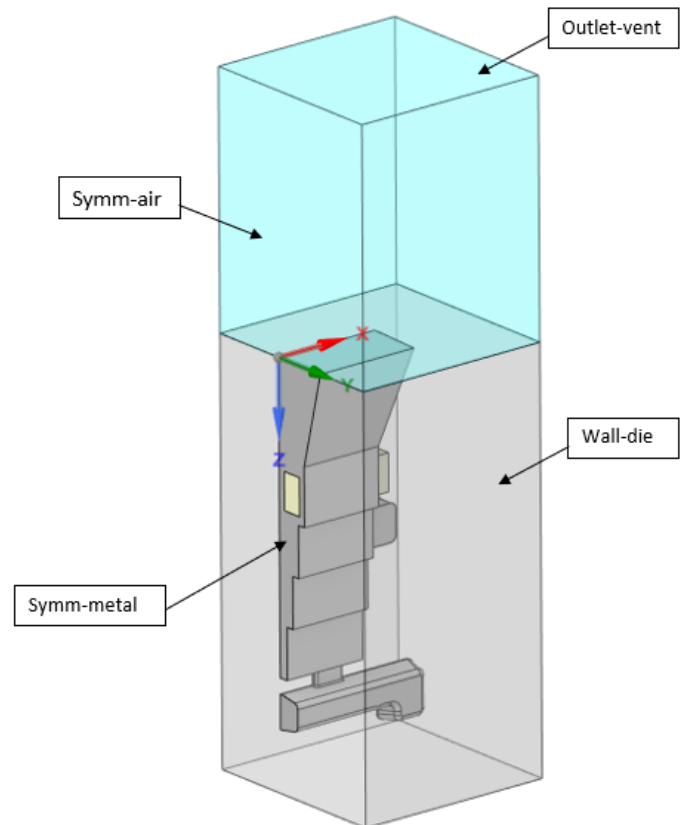


Figure 54

## 7.4 Fluent results

During the solidification the pressure field at the interface between the bar and the solidifying metal changes progressively because the density of the fluid increases with its cooling. Thermal conductivity of the sand agglomerate is low in the entire defined temperature range, so a certain time is expected to pass before the core region of the bar is warm enough to generate a general degradation of mechanical characteristics. Furthermore, a metal shrinkage is expected due to the density increase because of temperature decrease. The “Fluent” section simulates a time equal to 42 seconds, that is necessary to allow complete solidification of metal at the interface with the core (Figure 55).

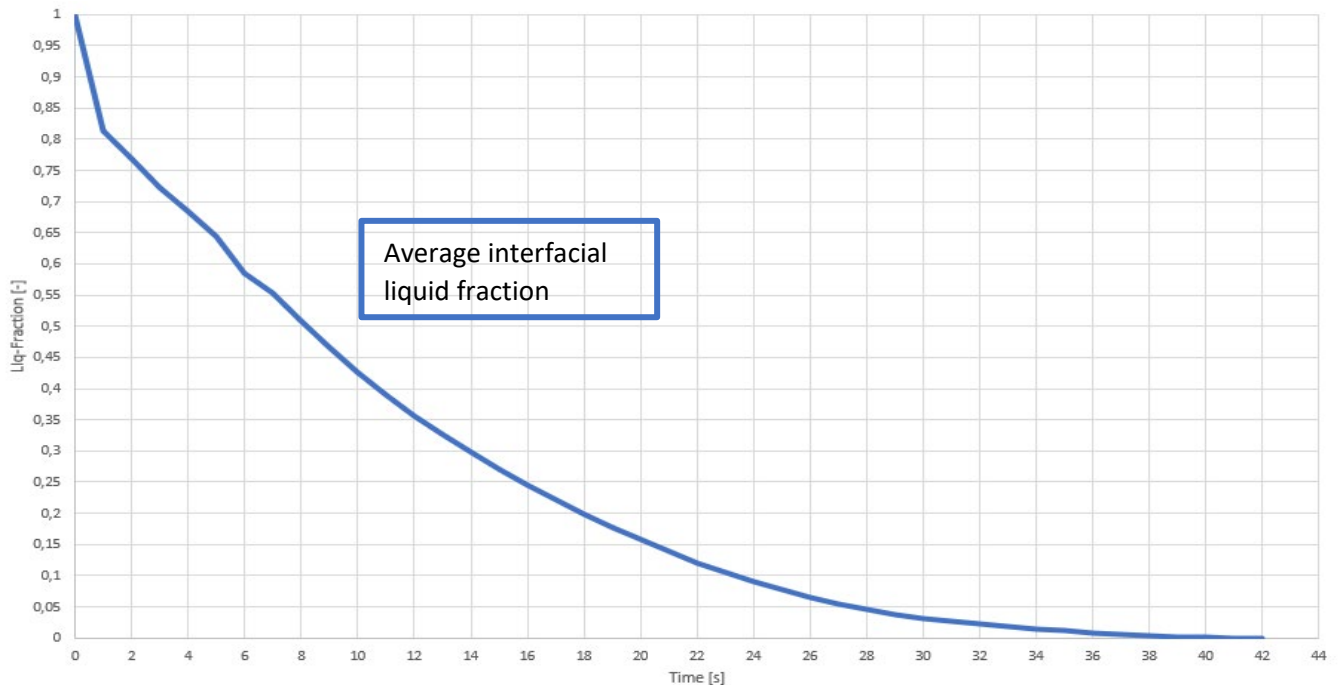


Figure 55: trend of liquid fraction at interface of the sand core bar with metal

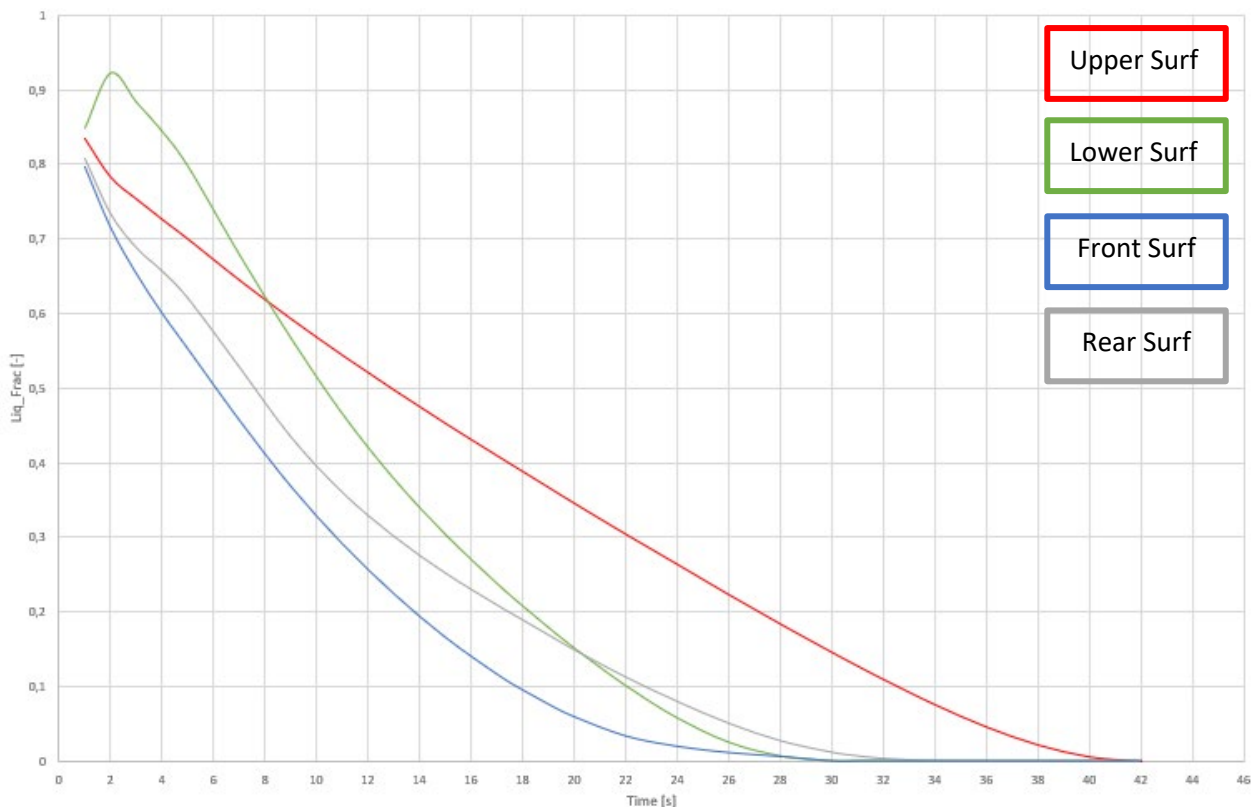


Figure 56: trends of average liquid fraction on each face

As shown in Figure 56 the solidification of molten aluminum on the upper face is sensibly slower with respect to the other faces in fact the region above the bar occupied by the fluid is much thicker and so the cooling and solidification rate are lower. Furthermore, solidification happens basically from the outer part towards the symmetry face, and it can be considered as an effect of the presence of the symmetry itself that implies adiabatic condition.

As in the previous simulation a deeper analysis has been performed to evaluate the force in Z direction (Figure 55). In this specific case pressure field variability, all around the bar, is expected to mainly derive by the change in density and, in a very limited portion, the fluid motion due to buoyancy effect. The results of the averaged total pressure trends are showed in Figure 57.

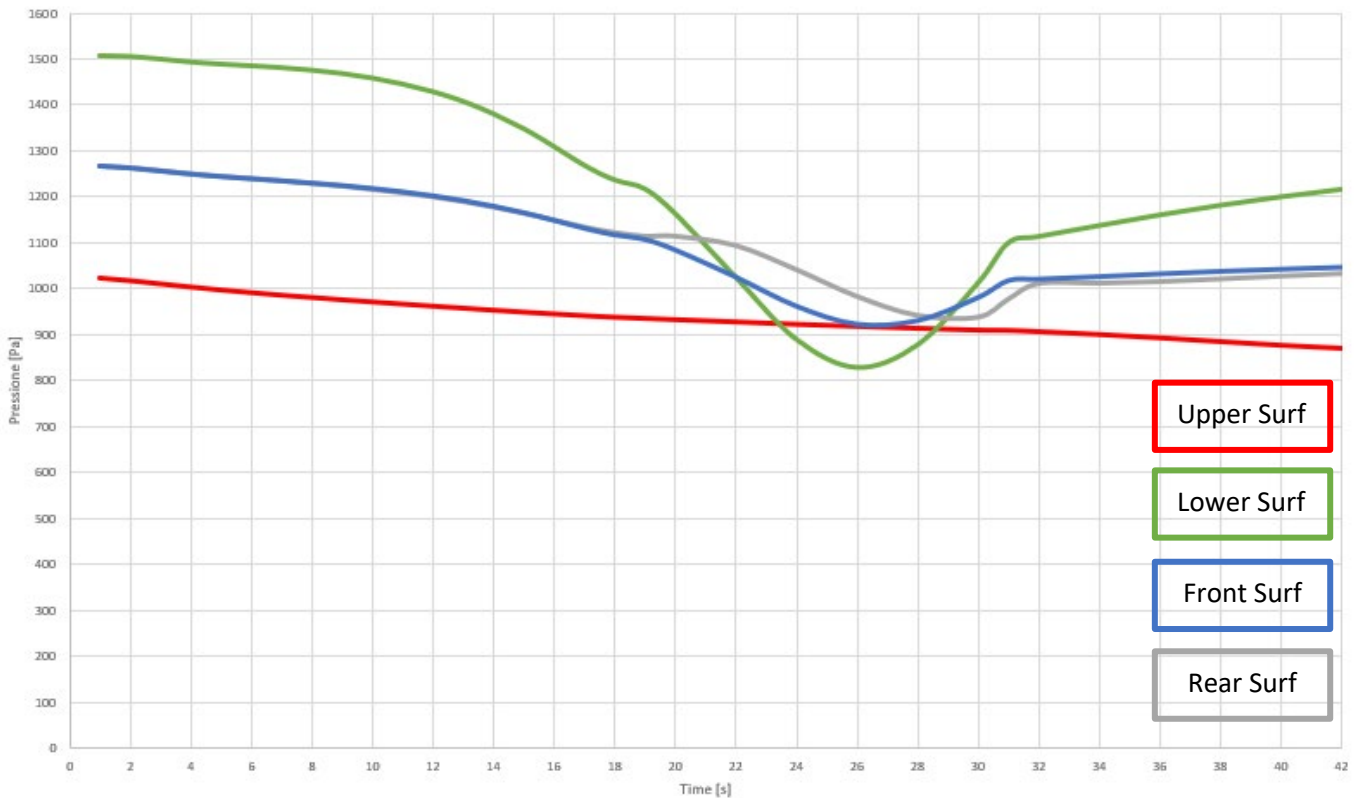


Figure 57: Averaged pressure trends on the separated interfaces

An unexpected behavior is monitored on the lower and lateral faces, in fact all three trends are quite stepping with a sudden fall and a later increase when the liquid fraction is very low. It seems not to have a direct and clear correlation with the fraction of the solidifying phase, that decreases monotonically and smoothly in all the regions of contact between the bar and the molten metal. A general pressure decrease can be associated with the management technique of solidification process, performed by the software that treats the mushy regions (coexistence of solid and liquid phases) as porous medium where the value of porosity is equal to the liquid fraction. When a region is completely solidified velocities are extinguished. So, the pressure drop can depend on the porous structure built during computational activity. The last unexpected increase of pressure in the lower face starts at the 26<sup>th</sup> simulated second. A possible reason can be assumed to be the complete solidification of regions all along the lateral faces of the bar that isolate the area not yet completely solidified just below the bar, creating a discontinuity in the liquid phase that surrounds the interface (Figure 58).

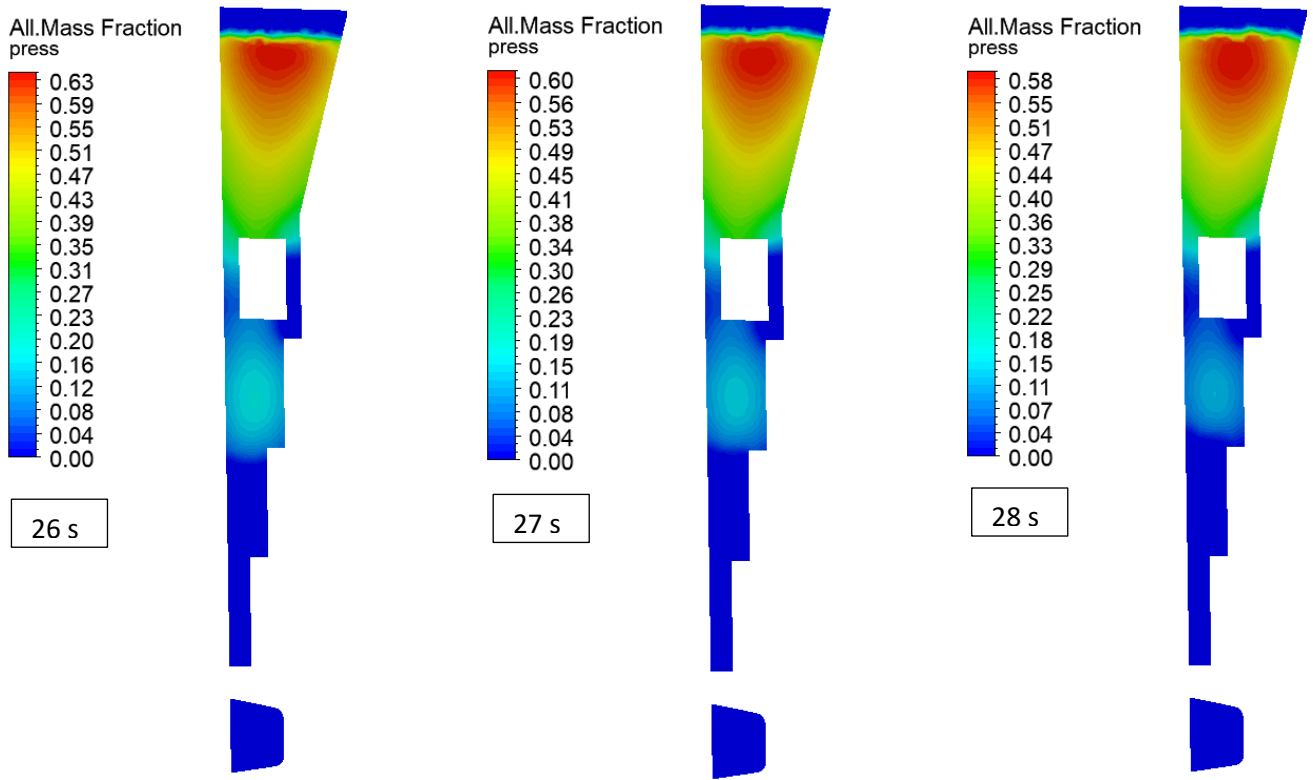


Figure 58: evolution of aluminum mass fraction on symmetry plane

As a direct consequence of this strange behavior also the resultants of the forces are strange. Forces in Z direction and their resultant are shown in Figure 59. Even if also forces on lateral faces show an inexplicable trend, average pressure has a quiet similar development, so a small lateral resultant force is anyway expected. Pressure field cannot be considered reliable and the forces that are directly computed by the software as the integral of pressure on the surface, are not reliable too.

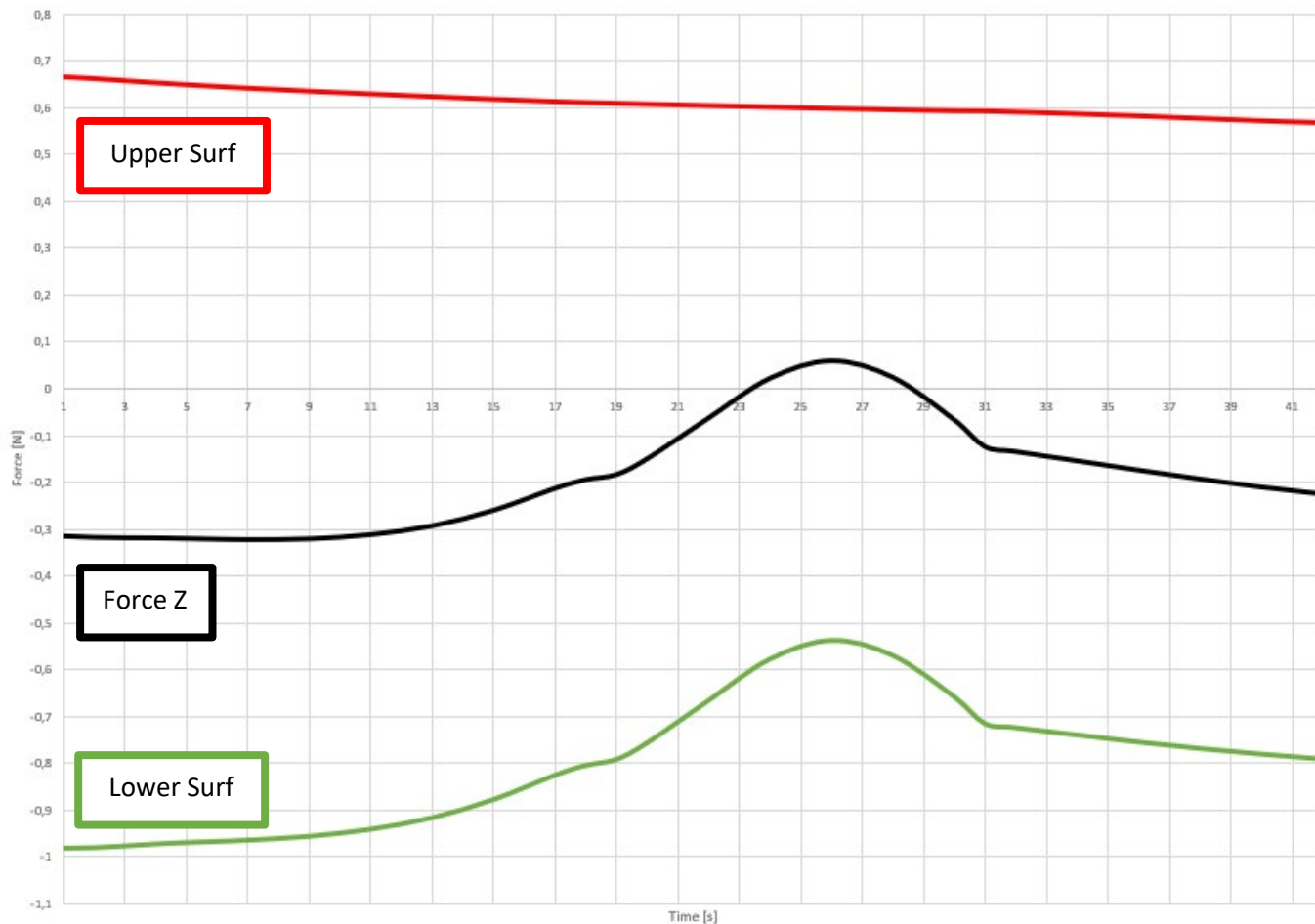


Figure 59: Force in Z direction

## 7.5 Static Structural

As in previous simulations geometry is only constituted by a half of the bar, with symmetry, and just a small portion of the entire die. The pressure field has been loaded to analyze the consequential deformation, especially in Z direction. In this case, differently from the previous ones also the thermal field of the bar has been imported from “Fluent”. In “Engineering Data” section the Young’s modulus has been defined as temperature dependent and so also this aspect has been affected the deformation. In this specific case an extension of the temperature range has been necessary with respect to the original one because the maximum temperature reached by the bar during the solidification is higher than 480 °C (Figure 61). The vertical deformation (Figure 60) is monitored with a probe in the center of the lower edge of the symmetry plane also in this case.

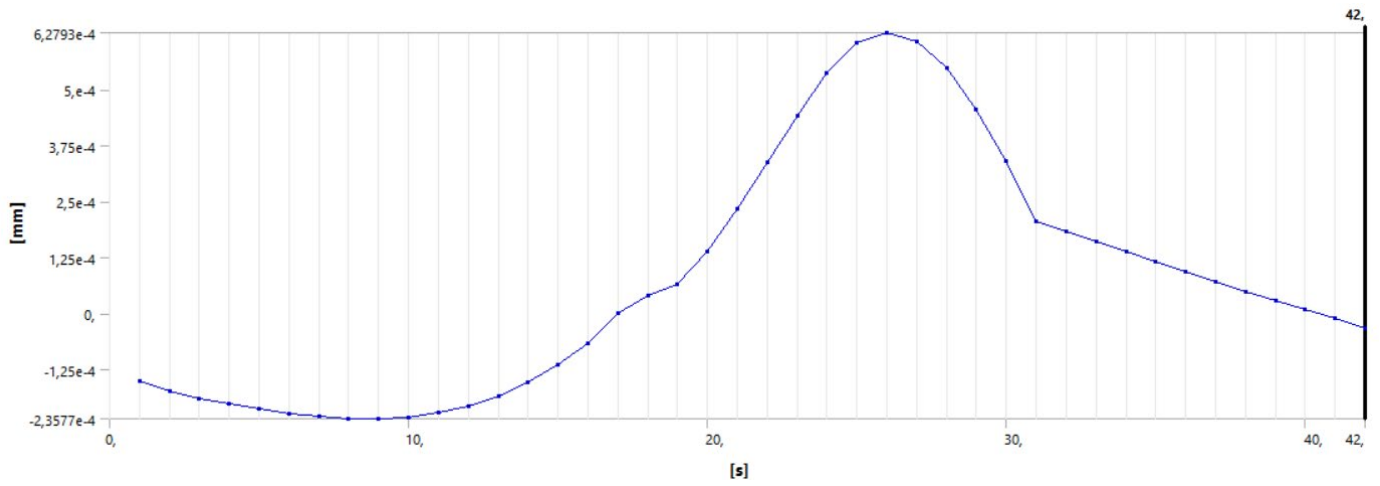


Figure 60: Z-directional displacement of the probe

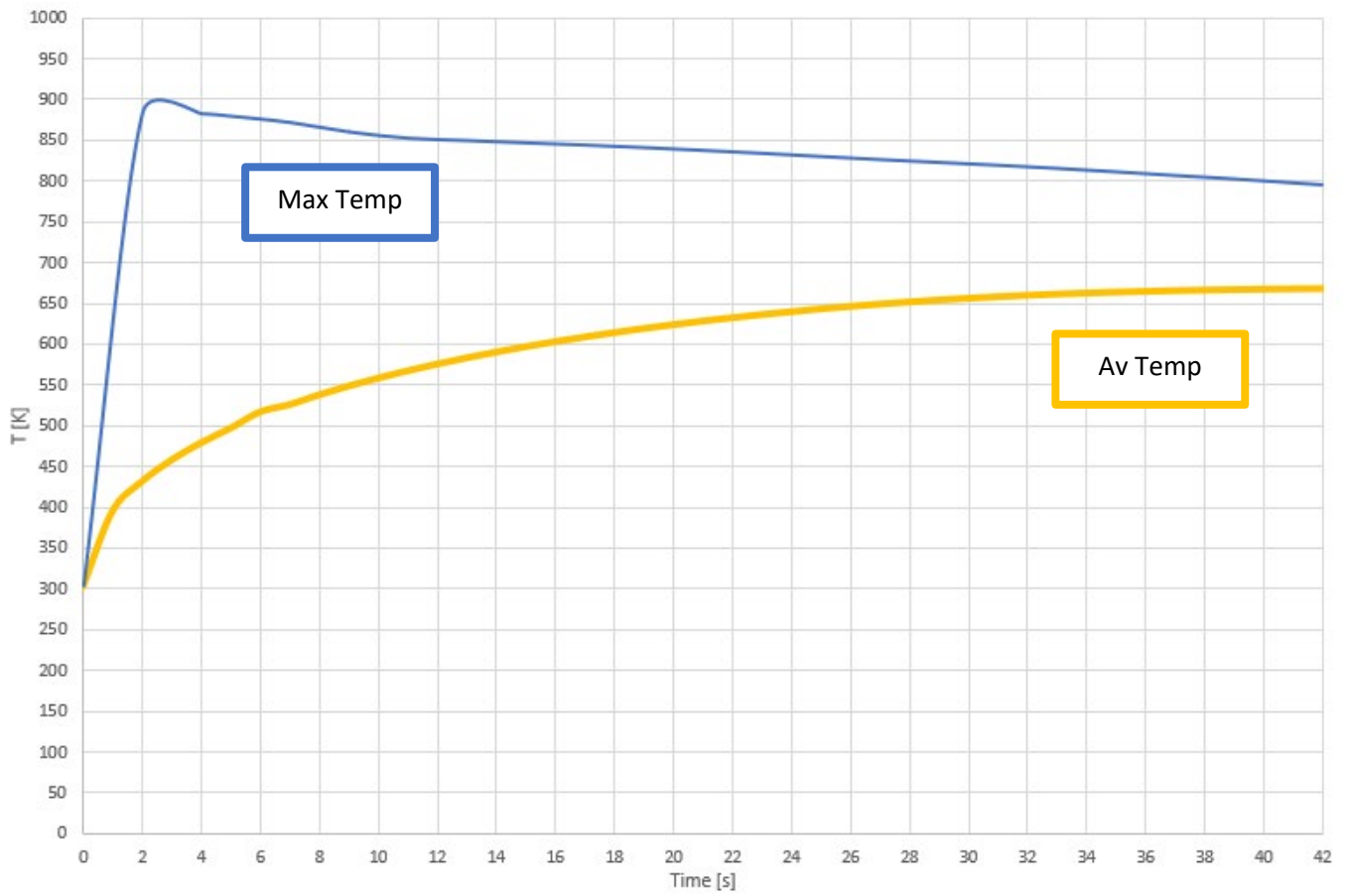


Figure 61: average and maximum temperature trends in the bar

## 8. CONCLUSION

This thesis work can be considered as an introduction of characterization of sand-binder agglomerates devoted to the core production. A possible testing approach, and a statistical method to define mechanical characteristics have been presented. A sure possible improvement to enhance the reliability of the obtained data can be related to the number of available specimens for each temperature; for this work only a total of 19 sand bars have been tested in a wide range of temperature (25 – 480 °C). Furthermore, a wider range with a higher maximum temperature seems to be necessary to characterize the agglomerate. Results of solidification show that even if the average temperature has an asymptotic behavior, stabilizing below the maximum threshold, some regions of the bar especially in proximity of the interface with metal reach a temperature quite above 480 °C, so additional mechanical data are necessary for a complete characterization.

Deformation of core due to the impingement of fluid metal is really small so the whole pouring phase, and even more the initial part of the solidification when the metal is almost rest and the bar mechanical characteristics are not deteriorated yet, cannot be considered as critical for the quality of the casting product. Anyway the casting product and core geometries are only suitable for tests, so a possible step over could be the analysis of a more complex and realistic geometry with thinner cores.

Before doing that, other possible enhancements can be:

- the extension of the solidification analysis to the whole geometry avoiding the usage of symmetry that is not fully appropriate due to the presence of pouring cone region and it would guarantee a more realistic temperature field evolution and thermal exchanges.
- a deeper comprehension of pressure development in solidifying fluid.
- the development of a system that constrains the bar considering the formation of solidified areas that limit more strictly the bar motion.
- an increase of testing specimens number because for this work only 19 sand bars were available for a really wide range of temperature. Furthermore, the temperature range has to be enlarged at least until the liquidus temperature of the aluminum alloy. So, an higher number of specimens is useful to make the statistical adopted process more realistic and reliable.

## REFERENCES

- [1] ASTM International. Designation: D 5934 – 02. Standard Test Method for Determination of Modulus of Elasticity for Rigid and Semi- Rigid Plastic Specimens by Controlled Rate of Loading Using Three-Point Bending.
- [2] Chu, Yunn-Kuang, and Jau-Chuan Ke. "Computation Approaches for Parameter Estimation of Weibull Distribution." *Mathematical and Computational Applications* 17, no. 1 (April 1, 2012): 39–47. <https://doi.org/10.3390/mca17010039>.
- [3] Czerwinski, F., M. Mir, and W. Kasprzak. "Application of Cores and Binders in Metalcasting." *International Journal of Cast Metals Research* 28, no. 3 (May 2015): 129–39. <https://doi.org/10.1179/1743133614Y.0000000140>.
- [4] Danko, Zych. "Diagnostic methods of technological properties and casting cores quality". *Archives of metallurgy and materials*. Faculty of foundry engineering, agh University of Science and Technology, 30-059 Krakow, 23 Reymonta str., Poland.
- [5] Danzer, Robert. "A General Strength Distribution Function for Brittle Materials." *Journal of the European Ceramic Society* 10, no. 6 (January 1992): 461–72. [https://doi.org/10.1016/0955-2219\(92\)90021-5](https://doi.org/10.1016/0955-2219(92)90021-5).
- [6] Holtzer, Mariusz, and Angelika Kmita. *Mold and Core Sands in Metalcasting: Chemistry and Ecology: Sustainable Development*. Cham: Springer International Publishing, 2020. <https://doi.org/10.1007/978-3-030-53210-9>.
- [7] Jain, Rahul, James Lock, and Stephen F. Duffy. "Effective Area and Effective Volume Calculations for Ceramic Test Specimens." In *Volume 1: Aircraft Engine; Ceramics; Coal, Biomass and Alternative Fuels; Controls, Diagnostics and Instrumentation; Education; Electric Power; Awards and Honors*, 231–39. Orlando, Florida, USA: ASME, 2009. <https://doi.org/10.1115/GT2009-59028>.
- [8] Morrell, Roger. "Measurement Good Practice Guide No. 7," n.d., 74.
- [9] Nohut, Serkan, Chunsheng Lu, and Lovro Gorjan. "Optimal Linear Regression Estimator in the Fitting of Weibull Strength Distribution." *Journal of Testing and Evaluation* 42, no. 6 (November 2014): JTE20130074. <https://doi.org/10.1520/JTE20130074>.
- [10] Stachowicz, M., K. Granat, and D. Nowak. "Application of Microwaves for Innovative Hardening of Environment-Friendly Water-Glass Moulding Sands Used in Manufacture of Cast-Steel Castings." *Archives of Civil and Mechanical Engineering* 11, no. 1 (January 2011): 209–19. [https://doi.org/10.1016/S1644-9665\(12\)60184-8](https://doi.org/10.1016/S1644-9665(12)60184-8).
- [11] Stauder, Bernhard J., Hubert Kerber, and Peter Schumacher. "Foundry Sand Core Property Assessment by 3-Point Bending Test Evaluation." *Journal of Materials Processing Technology* 237 (November 2016): 188–96. <https://doi.org/10.1016/j.jmatprotec.2016.06.010>.
- [12] Valencia, Juan J, and Peter N Queded. "Thermophysical Properties," n.d., 14.
- [13] Weissenbek, Emmerich, Thomas Kautz, Jörg Brotzki, and Jens Müller. "Tomorrow's Cylinder Head Production Ecology, Economy and Material Enhancement Brought in Line." *MTZ Worldwide* 72, no. 6 (June 2011): 48–53. <https://doi.org/10.1365/s38313-011-0064-7>.